The MFN2 Q367H variant from a patient with late-onset distal myopathy reveals a novel pathomechanism connected to mtDNA-mediated inflammation.

Mashiat Zaman[1], Govinda Sharma[2*], Walaa Almutawa[2*], Tyler GB Soule[3], Rasha Sabouny[2], Matt Joel[3], Gerald Pfeffer[4#], Timothy E. Shutt[4#]

[1]Department of Biochemistry & Molecular Biology, Cumming School of Medicine, Hotchkiss Brain Institute, University of Calgary

[2]Department of Biochemistry & Molecular Biology, Cumming School of Medicine, University of Calgary

[3]Department of Neuroscience, Cumming School of Medicine, Hotchkiss Brain Institute, University of Calgary

[4]Hotchkiss Brain Institute, Department of Clinical Neurosciences; and Alberta Child Health Research Institute, Department of Medical Genetics, Cumming School of Medicine, University of Calgary

[5]Departments of Medical Genetics and Biochemistry & Molecular Biology, Cumming School of Medicine, Hotchkiss Brain Institute, Snyder Institute for Chronic Diseases, Alberta Children's Hospital Research Institute; University of Calgary

*Equal contribution

[#]Corresponding authors

Abstract

Background

MFN2 encodes a multifunctional mitochondrial protein best known for its role mitochondrial fusion. While pathogenic variants in *MFN2* typically cause Charcot-Marie-Tooth disease subtype 2A, an axonal peripheral neuropathy, exome sequencing identified an uncharacterized *MFN2* variant, Q367H, in a patient diagnosed with late-onset distal myopathy without peripheral neuropathy. Although impaired mitochondrial fusion can cause mtDNA-mediated inflammation via TLR9 activation of NF-kB, which is linked to myopathy in a mouse model of MFN1 deficiency, this pathway has not yet been functionally linked to *MFN2* pathology.

Methods

To investigate if the Q367H MFN2 variant contributes to the patient phenotype, we applied several biochemical and molecular biology techniques to characterize patient fibroblasts and transdifferentiated myoblasts for several functions mediated by MFN2. We also examined TLR9 and cGAS-STING mtDNA-mediated inflammatory pathways.

Findings

Patient fibroblasts showed changes consistent with impairment of several MFN2 functions. When grown in standard glucose media, patient fibroblasts had reduced oxidative phosphorylation and elevated levels of lipid droplets. When grown in galactose media, patient fibroblasts had fragmented mitochondria, reduced mito-ER contact sites, and enlarged mtDNA nucleoids. Notably, under both media conditions, mtDNA was present outside of the mitochondrial network, where it co-localized with early endosomes. We also observed activation of both TLR9/NF-kB and cGAS-STING inflammation in fibroblasts. Moreover, the inflammatory signaling was increased 3-10 fold in transdifferentiated patient myoblasts, which also exhibited reduced mito-ER contacts and altered mtDNA nucleoids.

Interpretation

We report a patient with myopathy, but without the typical peripheral neuropathy associated with *MFN2* disease variants. As elevated inflammation can cause myopathy, linking the Q367H MFN2 variant with elevated TLR9 and cGAS/STING signaling, which is amplified in transdifferentiated myoblasts, provides novel insight into the patient's phenotype. Thus, we establish a potential novel pathomechanism connecting MFN2 dysfunction to mtDNA-mediated inflammation.

51 **Introduction**

52 Mitochondria are highly dynamic cellular structures that fuse, divide, move about the cell, and
53 interact with other organelles. The integral outer-mitochondrial-membrane (OMM) proteins Mitofusin1
54 (MFN1) and Mitofusin 2 (MFN2) mediate fusion of the outer mitochondrial membrane. MFN2, though
55 named for its role in mitochondrial fusion, is also actively involved in several other dynamic processes
56 (1): it mediates contacts between mitochondria and the endoplasmic reticulum (ER) (2), referred to here
57 as mito-ER contact sites (MERCs); is involved in mitochondrial interactions with lipid droplets (3), early
58 endosomes (4), and the nucleus (5); and also plays an active role in mitochondrial autophagy
59 (mitophagy) (6,7).

60 Pathogenic variants in MFN2 are typically associated with the axonal peripheral neuropathy
61 Charcot-Marie-Tooth disease subtype 2A (CMT2A). Characterized by weakness, numbness and pain in
62 the distal regions of the body, CMT2A is often an early-onset progressively-worsening disease (8). In
63 addition to peripheral neuropathy, patients with certain MFN2 variants can present with other
64 pathogenic phenotypes, such as myopathy (9–11), optic atrophy, sensorineural hearing loss, ataxia (12),
65 or multiple symmetric lipomatosis (MSL) (13–15). How and why different variants in MFN2 lead
66 mechanistically to pathology is not fully understood, though it is likely not as simple as reduced
67 mitochondrial fusion (16).

68 In addition to its critical role in neurons, MFN2 is also important for muscle function. Muscle-
69 specific MFN2 knockout results in muscle atrophy, which is attributed to loss of mitochondrial fusion and
70 subsequent instability of the mitochondrial genome (mtDNA) (17). On top of the depletion of mtDNA
71 copy number that is thought to contribute to respiratory deficiency, mtDNA can accumulate point
72 mutations and deletions in the muscle tissue of these KO mice. A role for MFN2 in maintaining mtDNA is
73 further supported by the fact that certain pathogenic *MFN2* variants show a reduction in mtDNA copy
74 number (18,19) or lead to mtDNA deletions (20). However, highlighting our incomplete understanding of
75 the pathology caused by MFN2 deficiency and the role played by mtDNA, not all pathogenic *MFN2*
76 variants impair mitochondrial fusion, impact mtDNA, or cause respiratory deficiency (16).

77 Beyond its role of encoding OXPHOS proteins, mtDNA is now also recognized to play an
78 important role as an inflammatory signalling molecule when released from mitochondria. Examples of
79 inflammatory signalling pathways that detect mtDNA-mediated include TLR9 (4,18), cGAS-STING (21,22)
80 and the inflammasome (23,24). Notably, a recent study showed that inducible muscle-specific loss of
81 MFN1 causes mtDNA release via early endosomes, leading to activation of TLR9/NF-kB inflammation and
82 myopathy (4). Importantly, pharmacological inhibition of this inflammation improved the muscle atrophy

83 and physical performance in these mice, implicating sterile inflammation in the muscle pathology of
84 these mice. Nevertheless, the role of mtDNA-mediated inflammation in the pathology of pathogenic
85 *MFN2* variants has not been described to date.
86 Here we report a novel MFN2 variant, Q367H, in a patient diagnosed with late onset distal
87 myopathy. Functional characterization of patient fibroblasts and transdifferentiated myoblasts reveals
88 mtDNA-mediated TLR9 signaling that likely explain the patient myopathy, thus expanding our
89 understanding of the mechanisms by which MFN2 dysfunction contributes to pathology.
90
91
92 **Methods**
93 Ethics statement
94 The patient provided written informed consent for participation in research and consented to
95 the publication of this report. He was provided with a copy of the draft article prior to submission.
96 Genetic sequencing and human tissue studies with this participant were part of research protocols
97 (REB15-2763 and REB17-0850) approved by the Conjoint Health Research Ethics Board at the University
98 of Calgary.
99
100 Exome Sequencing, Variant Confirmation and Sequence Conservation Study
101 DNA was extracted from blood collected into EDTA tubes using standard protocols. Library
102 preparation proceeded using the Ion Ampliseq Exome RDY Panel (Thermo Fisher, A38264) according to
103 manufacturer's protocol. Automated chip loading and templating used the Ion Chef system and 540
104 chip/chef kit (Thermo Fisher, A30011), and sequencing was performed on an Ion S5 system (Thermo
105 Fisher, A27212), according to manufacturer's protocols. Base calling, read alignment to hg19, coverage
106 analysis, and variant calling were performed with Torrent Suite (v. 5.10.1; Thermo Fisher). Similar
107 analysis can be performed using an alternative bioinformatic pipeline as described previously (25).
108 Patient VCFs were annotated for predicted variant consequence, gnomAD allele frequency, CADD score,
109 and OMIM phenotypes, in addition to default parameters with Ensembl's command line Variant Effect
110 Predictor (VEP). We additionally aligned off-target reads from exome sequencing to identify any mtDNA
111 variants, as previously described (26).
112 The variant was verified by Sanger sequencing. Briefly, total genomic DNA was collected using
113 the E.Z.N.A Tissue DNA Extraction Kit (VWR, CA101319-018). The region of interest was amplified using
114 PCR with the following primers (F-GAGAAGAGCAGAGAGGCTCTTG and R-ACACAGGGAATCGTGCTGC).

115 Subsequently the amplified region was sequenced by Sanger sequencing at University of Calgary Centre
116 For Health Genomics And Informatics.
117 Amino acid sequence alignment was performed using the T-COFFEE online tool (27). The
118 sequences were collected from UniProt(28). The following accession codes were used for the sequences:
119 MFN2: O95140-1, MFN1: Q8IWA4, Mouse MFN2: Q80U63, Fish MFN2: A8WIN6, Chicken MFN2: E1BSH7,
120 Frog MFN2: Q28CS2, Fruit fly MFN: Q7YU24, Worm MFN: Q23424.
121
122 Quantification of Protein Amounts:
123 Relative quantities were measured using Western Blot Analysis, as previously described (12).
124 Briefly, cells were lysed with Pierce RIPA buffer (Thermo Scientific™, 89900), and subsequently total
125 protein was quantified by a BCA assay. 50 µg of protein was loaded from control and patient fibroblasts
126 on to an SDS-PAGE gel. After running the gel, the blots were transferred to a PVDF membrane overnight.
127 The blots were probed using the following antibodies: anti-MFN2 (Abnova, H00009927-M03; 1:1000),
128 anti-MFN1 (Cell Signaling Technology, D6E2S; 1:1000), anti-OPA1 (BD Transduction Laboratories, 612607;
129 1:1000), anti-Actin (Sigma, A5316; 1:1000). Secondary antibodies complimentary to the primary host
130 species were used- goat anti-rabbit IgG, HRP linked Antibody (Cell Signaling Technology, 7074S) or goat
131 anti-mouse IgG-HRP (Santa Cruz Biotechnology, sc-2055). The membranes were visualized with
132 SuperSignal™ West Femto Maximum Sensitivity Substrate (Thermo Scientific™, 34095) using the Bio-Rad
133 ChemiDoc Imaging System. Bands were quantified using Fiji (29).
134
135 Cell Culture and Maintenance
136 Fibroblasts from the patient and healthy individual were generated through skin biopsies as
137 described (25). The cells were cultured using Minimum Essential Media (Gibco, 11095080),
138 supplemented with 10% Fetal Bovine Serum and 1mM Sodium Pyruvate. Glucose-free conditions were
139 established using DMEM No Glucose media (Gibco, 11966025), supplemented with 5mM galactose, 10%
140 FBS and 1mM Sodium Pyruvate. Cells were grown in an incubator, maintained at 37°C and 5% CO_2. For
141 the fatty acid pulse-chase assay, the cells were grown in the glucose media mentioned above, or glucose-
142 free media with 10% FBS, but no galactose.
143
144 Mitochondrial Morphology Analysis
145 Mitochondrial morphology was analyzed by immunostaining as described previously (30), where
146 30,000 cells were grown in 12mm coverslips for 24 hours and subsequently fixed by 4% PFA for 20

147 minutes at 37°C. Cells were permeabilized using 0.1% Triton X-100 (MP Biomedicals, J00105) and
148 blocked using 5% FBS. The OMM protein TOMM20 was chosen to visualize the mitochondrial network,
149 where cells were incubated with mouse anti-TOMM20 (Santa Cruz Biotechnology, F-10, RRID:
150 AB_628381) overnight, the subsequently probed with goat anti-mouse secondary conjugated with Alexa
151 fluor 488 (Thermo Fisher Scientific, A-11029). Cover slips were then mounted on glass slides using
152 ProLong Diamond Antifade Mountant with DAPI (Invitrogen, P36966).
153
154 Oxygen Consumption Rate
155 The cellular oxygen consumption rate assay for control and patient fibroblasts was performed as
156 previously described (31). Briefly, 40,000 cells were seeded in wells of the XF-24 plates (Agilent). The
157 media on the plates was replaced 24 hours later with Seahorse CF Base Medium, supplemented with
158 1mM Pyruvate, 2mM Glutamine and 10mM Glucose and brought to pH 7.4. Post-incubation for 45
159 minutes with CO_2, cells were loaded into the Seahorse XF24 Analyzer. Oxygen consumption rates were
160 measured at three time points, following administration of Oligomycin (0.5 µM), Carbonyl cyanide-p-
161 trifluoromethoxyphenylhydrazone (FCCP) (1 µM) and Antimycin A (0.5 µM). Following the experiment,
162 cells in each well were lysed with Pierce RIPA buffer and total protein for each well was quantified with
163 BCA assays, for normalization purposes.
164
165 mtDNA and Mitochondrial Nucleoid Analyses
166 Mitochondrial nucleoids were visualized using confocal microscopy as previously reported (32).
167 Briefly, 30,000 control and patient fibroblasts were grown on coverslips for 24 hours and fixed with 4%
168 PFA. Cells were permeabilized with 0.2% Triton X-100 and blocked with 5% FBS. Mitochondrial nucleoids
169 were labelled using mouse anti-dsDNA antibody (Developmental Studies Hybridoma Bank,
170 AB_10805293, RRID:AB_10805293) and subsequently visualized using the goat anti-mouse secondary
171 conjugated with Alexa fluor 488. The mitochondrial network was also labelled using anti-rabbit TOMM20
172 rabbit anti-TOMM20 (Abcam, ab186735), which was visualized with anti-Rabbit secondary conjugated
173 with Alexa fluor 647 (Thermo Fisher Scientific, A-21245). Cover slips were mounted using ProLong
174 Diamond Antifade Mountant with DAPI.
175 mtDNA copy number analysis was performed using qPCR. Total DNA was collected from control
176 and patient fibroblasts seeded at the same density. Relative mtDNA copy number was analyzed using
177 nuclear-encoded housekeeping gene 18S, by amplification using the following primers:
178 mito-F- CACCCAAGAACAGGGTTTGT

179 mito-R- TGGCCATGGGTATGTTGTTAA

180 18S-F- TAGAGGGACAAGTGGCGTTC

181 18S-R- CGCTGAGCCAGTCAGTGT

182 For qPCR, 50ng of total DNA was loaded into each well a 96-well plate and the reaction was
183 performed using the QuantStudio6 Flex Real-Time PCR system (Thermo Fisher Scientific). The delta Ct
184 method was used to determine the relative copy number.

185 Long range PCR was done to look for mtDNA deletions using the Takara LA Taq Polymerase
186 (Takara Bio, RR002M). Total DNA was collected from control and patient fibroblasts and 16.2kBP
187 fragment was amplified using the following primers- (F- ACCGCCCGTCACCCTCCTCAAGTATACTTCAAAGG
188 and R- ACCGCCAGGTCCTTTGAGTTTTAAGCTGTGGCTCG). Long Range PCR was done using the following
189 conditions- (94 °C for 1 min; 98 °C for 10 s, and 68 °C for 11 min (30 cycles), followed by a final extension
190 cycle at 72 °C for 10 min). The products following the reaction were visualized by gel electrophoresis on a
191 0.6% gel run for 18 hours at 18V.

192

193

194 Mito-ER Contact Sites

195 The proximity ligation assay was used to look for MERCs, using the Duolink In Situ Detection kit
196 (Sigma Aldrich, DUI92008). Briefly, 30,000 control and patient cells were grown on coverslips for 24
197 hours and subsequently fixed using 4%PFA. Cells were permeabilized with 0.1% Triton X-100 and blocked
198 using the blocking reagent provided by the kit. The cells were then incubated overnight using mouse-
199 anti-Calnexin (Sigma-Aldrich, MAB3126) and rabbit anti-TOMM20 (Abcam, ab186735). Following
200 incubation, PLA probes, complementary to the primary antibodies, anti-mouse (Sigma-aldrich,
201 DUO92004) and anti-rabbit (Sigma-aldrich, DUO92002) were added to the coverslips. The addition of
202 DNA ligase and DNA polymerase were subsequently carried out using manufacturer's instructions and
203 using the reagents provided in the kit. Finally, secondary antibodies anti-mouse secondary conjugated
204 with Alexa fluor 488 (Thermo Fisher Scientific, A-11029) and anti-Rabbit secondary conjugated with
205 Alexa fluor 647 (Thermo Fisher Scientific, A-21245) were added for visualizing the ER and mitochondrial
206 networks respectively. The coverslips were mounted with ProLong Diamond Antifade with DAPI before
207 imaging.

208

209 Lipid Droplets and Fatty Acid Pulse-Chase

210 Total cellular lipid droplets were labelled using HCS LipidTox Green (Thermo Fisher Scientific,
211 H34350), following the same immunostaining protocol to label the mitochondrial network, except for
212 using 0.1% Saponin (Sigma Aldrich, SAE0073-10G) as the permeabilizing solution. The mitochondrial
213 network was also labelled using anti-rabbit TOMM20 rabbit anti-TOMM20 (Abcam, ab186735), which
214 was visualized with anti-Rabbit secondary conjugated with Alexa fluor 647 (Thermo Fisher Scientific, A-
215 21245).
216 For the fatty acid pulse-chase assay, 50,000 cells were seeded on a 35mm glass bottom dish with
217 20mm indented imaging region. Cells were grown for 24 hours, after which they were pulsed with the
218 fluorescent fatty acid precursor BODIPY 558/568 C_{12} (Invitrogen, D3835). After 24 hours incubation with
219 the BODIPY, cells were incubated with either glucose or glucose-free media and chased at time points 0
220 hours, 6 hours and 24 hours following the addition of the two media conditions. When the variable
221 media conditions were added, MitoTracker Green (Invitrogen, M7514) was also added at 50nM
222 concentration for visualizing the mitochondrial network.
223
224 Mitochondria, mtDNA and Early Endosome Imaging
225 The triple staining of the mitochondrial network, mtDNA and early endosomes was performed
226 using sequential immunostaining. The steps until blocking are the same as described above for the
227 mitochondrial network. Following blocking, primary antibodies were added for the mtDNA (same as
228 above) and mitochondrial network (same as above) and secondary antibodies were added accordingly-
229 anti-mouse secondary conjugated with Alexa fluor 488 (Thermo Fisher Scientific, A-11029) and anti-
230 Rabbit secondary conjugated with Alexa fluor 568 (Thermo Fisher Scientific, A-11004). Following
231 secondary antibody incubation, coverslips were thoroughly washed with PBS and the primary antibody
232 to label early endosomes was added rabbit anti-RAB5 (Cell Signaling Technology, 3547T). Subsequently,
233 the complementary secondary antibody anti-Rabbit secondary conjugated with Alexa fluor 647 (Thermo
234 Fisher Scientific, A-21245) was added. The coverslips were mounted using ProLong Diamond Antifade
235 mounting media.
236
237 Fibroblast Transdifferentiation
238 The coding sequence for human myoD1 (accession NM_002478) was PCR amplified from a
239 human skeletal muscle cDNA library and subcloned into pWPXL (pWPXL was a gift from Didier Trono
240 (Addgene plasmid # 12257) in place of eGFP at the 5'BamHI and 3'EcoRI restriction sites. The DNA
241 sequence was confirmed using Sanger DNA sequencing.

242 Lentivirus production was performed using 293FT cells grown to 90% confluency on five, 15 cm^2
243 cell culture plates, by cotransfecting 112.5 µg pWPXL-myoD1, 73 µg psPAX2 and 39.5 µg pMD2.G [gifts
244 from Didier Trono (Addgene, plasmid # 12260) using PEIpro transfection reagent (Polyplus). The cell
245 culture media was collected 48 hours post-transfection, quantified using Lenti-X™ GoStix™ Plus (Takara
246 Bio USA, 631280), centrifuged at 500xg for 5 min, 0.45 um filtered and stored at -80°C as 5 mL aliquots.
247 Non-immortalized primary fibroblasts below passage 5 were grown at 37°C, 5% CO_2 in complete
248 media: DMEM – high glucose (Corning, 10-013-CV), 10% FBS (Corning, 35-077-CV), 1% P/S (VWR, K952).
249 T75s or 24 well plates were coated in 0.1 mg/mL VitroCol Type I human collagen (Advanced BioMatrix,
250 5008) for 1 hour before gently washing with PBS. Cells were seeded at 6,300/cm^2 and transduced at 75%
251 confluency. 5 µg/mL polybrene (Sigma-Aldrich, TR-1003-G) was mixed with MYOD1 lentivus at GoStix
252 Values of either 11,500 or 12,000 depending on the biological replicate. Cells were transduced by
253 spinfection, specifically a one-hour spin at 800 xg, RT, and then lentiviral supernatant was replaced with
254 complete media. Media was changed every two days and cells were allowed to transdifferentiate for 7
255 days before fixing or RNA extraction. Conversion to myoblasts was confirmed by visualization of Desmin
256 using Desmin (D93F5) XP Rabbit mAb (CST, cat. #5332S) and secondary AlexaFluor 594 chicken anti-
257 rabbit (Invitrogen, A-21442). RNA for qPCR was extracted using RNeasy Mini Kit (QIAGEN, 74104).
258
259 Analysis of TLR9-NF-kB Signalling Pathways:
260 The expression of genes associated with the TLR9-NF-kB was analyzed by RT-qPCR. The TLR9
261 inhibitor Chloroquine (MilliporeSigma, C973P63) and the cGAS-STING inhibitor Ru.521 (Aobious,
262 AOB37877) were added to the cell culture media (final concentration 1uM) for 24 hours, and
263 subsequently the cells were washed five times with PBS. Briefly, total RNA was extracted from cells using
264 the HP Total RNA Extraction Kit (VWR, CA101414-852), according to the manufacturer's instructions. The
265 collected RNA was reverse transcribed using the iScript Advanced cDNA Synthesis Kit (BioRad, 1725038).
266 Subsequently, qPCR was performed using the QuantStudio 6 Real-Time PCR system (Thermo Scientific).
267 The primers used for amplification of target genes are:
268 Beta Actin- F- AAGACCTGTACGCCAACACA
269 Beta Actin- R- AGTACTTGCGCTCAGGAGGA
270 Asc-F- CATGAACTGATCGACAGGATG
271 Asc-R- GGACCTCCTCCAAATGTTTC
272 IL6-F-- AGACAGCCACTCACCTCTTCAG
273 IL6-R- TTCTGCCAGTGCCTCTTTGCTG

274 Nlrp3-F- GCTGGCATCTGGATGAGGAA

275 Nlrp3-R- GTGTGTCCTGAGCCATGGAA

276 S100a9-F- GGAATTCAAAGAGCTGGTGC

277 S100a9-R- TCAGCATGATGAACTCCTCG

278 TNF-F- GCCCATGTTGTAGCAAACCC

279 TNF-R- GGAGGTTGACCTTGGTCTGG

280 IFN-α-F- AAATACAGCCCTTGTGCCTGG

281 IFN-α-R- GGTGAGCTGGCATACGAATCA

282 IFN-β-F- AAGGCCAAGGAGTACAGTC

283 IFN-β-R- ATCTTCAGTTTCGGAGGTAA

284

285 Imaging and Analyses

286 All imaging was performed as previously described (21). The Olympus Spinning Disk Confocal
287 System (Olympus SD OSR) was used with the UAPON 100XOTIRF/1.49 oil objective lens. For live cell
288 imaging, a cellVivo incubation module was used to maintain cells at 37°C and 5% CO_2. For analysis of
289 mitochondrial branch length and footprint, the MiNA plugin (33) was used on Fiji. Number and size of
290 PLA puncta, mitochondrial nucleoids and lipid droplets was performed using the particle analysis tool on
291 Fiji, following thresholding. All co-localization studies were performed using the JaCoP plugin (34) on Fiji.
292 All quantitative figures and statistical tests were performed using GraphPad Prism 9.

293

294 **Results**

295 **Patient Report, Whole Exome Sequencing and Protein Expression for MFN2 Q367H Variant**

296 A male patient in their 70s presented with a two-year history of slowly progressive weakness
297 affecting his lower extremities. Initial symptoms included difficulty walking uphill, and he eventually
298 developed difficulty with stairs and limitations with walking on the ground level and rising from a chair.
299 There were no cramps, fasciculations, or contractures. No sensory loss or coordination. Dysarthria,
300 dysphagia, ptosis, or diplopia were not present.

301 The patient was medically well and did not have any history of cardiac disease. The parent of the
302 proband developed weakness in her lower legs in her 60s, with progressive limitations in her mobility.
303 Apparently, she was diagnosed with CMT disease, but her clinical profile was not available for review.
304 The parent died in her early 80s due to congestive heart failure. The parent's two siblings aged 76-80,
305 and her other two children aged 40-45 were all unaffected. Clinical examination of the patient
306 demonstrated a cognitively normal individual. Cranial nerve examination was normal. Motor
307 examination revealed MRC grade 4+ strength for ankle dorsiflexion and 4+ plantarflexion bilaterally.
308 Proximal and axial muscle testing was normal, except for Achilles tendon reflexes. The sensory
309 examination was normal. Creatine kinase enzyme activity was elevated to a maximum of 455 U/L
310 (reference range ≤ 195 U/L). The muscle biopsy showed necrotic and regeneration myofiber, myofiber
311 hypertrophy, multifocal endomysia, and perimysial fibrosis, and extensive infiltration by adipose tissue.
312 Immunostaining for dystrophin, alpha/gamma sarcoglycan, sceptrin, α-laminin, desmin, and α-β-
313 crystallin was unremarkable. There was no inflammatory cell infiltrate. For the magnetic resonance
314 imaging (MRI) examination, upper and lower legs revealed atrophy in the adductor longus gluteus
315 minimus, tibialis anterior, and inferior gastro-soleus bilaterally [Figure 1A/B].

316 The case was interpreted as a chronic myopathy nonspecific muscle pathology. A genetic cause
317 was suspected given the family history of a similar condition in his parent, and lack of inflammation on
318 muscle biopsy. Clinical testing with a gene panel encompassing 200 genes associated with myopathy,
319 neuropathy, and neuromuscular disorders identified a previously uncharacterized heterozygous variant
320 in the *MFN2* gene, c.1101G>C, p. (Gln367His) [Table 1/Figure 1C]. Research based exome sequencing
321 again identified the *MFN2* variant, as well as heterozygous variants of unknown significance in *SYNE1*
322 and *DYSF* (Table 1). While pathogenic variants in *SYNE1* can be associated with autosomal dominant
323 neuromuscular disease, this patient variant was not considered to be clinically relevant for the following
324 reasons: (a) the variant is not in the same domain as pathogenic variants previously associated with
325 autosomal dominant disease, (b) *SYNE1* variants in this region of the gene have only been associated

326 with autosomal recessive disorders, while our patient is heterozygous, (c) no characteristic nuclear
327 abnormalities associated with pathogenic variants in *SYNE1* (35) were observed in patient fibroblasts
328 under microscopy, (d) the myopathy phenotype is not in keeping with the *SYNE1*-related disease
329 phenotype, which includes proximal weakness and contractures. Meanwhile, the *DYSF* variant was not
330 considered to be an explanation for this patient's disease because it is a single heterozygous variant in a
331 condition caused by biallelic variants in *DYSF*, and we are not aware of any reports of dysferlinopathy
332 associated with only a single pathogenic variant. Thus, based on strong suspicion for the relationship
333 between the *MFN2* variant and the patient phenotype, we proceeded with the studies described in this
334 report using patient fibroblast cells.
335
336 **Characterization of Patient Fibroblasts:**
337 To investigate if the Q367H variant contributes to the patient phenotype, we began by examining
338 skin fibroblasts obtained from the patient. Immunoblotting for mitochondrial fusion proteins revealed no
339 significant changes in the expression of MFN2, MFN1, or the inner mitochondrial membrane fusion
340 protein OPA1 (Figure 1E-J). Next, to determine if this MFN2 variant may contribute to the pathology and
341 to gain potential insight into the disease mechanism(s), we characterized patient fibroblasts for
342 alterations to a variety of MFN2-mediated functions.
343
344 **Mitochondrial Network Morphology and Respiration in MFN2 Q367H Fibroblasts**
345 First, as fibroblast cells from CMT2A patients with MFN2 variants sometimes have fragmented
346 mitochondria (16), we examined mitochondrial morphology as a potential downstream readout of
347 altered mitochondrial fusion (Figure 2A-C). No changes were observed under standard culture
348 conditions. However, glucose-free growth conditions supplemented with galactose, which forces cells to
349 use mitochondria for energy rather than glycolysis, can be used detect morphology changes in
350 fibroblasts from patients with MFN2 variants (36). Consistent with decreased mitochondrial fusion and
351 mitochondrial dysfunction, Q367H patient fibroblasts grown in glucose-free galactose-supplemented
352 media showed a marked increase in the number of cells with fragmented mitochondrial networks, as
353 well as a decrease in average mitochondrial length. Impairment of mitochondrial function in patient
354 fibroblasts was further reinforced by functional studies of oxygen consumption. Patient fibroblasts had
355 increased basal oxygen consumption but reduced maximal oxygen consumption (Figure 2D). As
356 mitochondrial fragmentation alone does not indicate MFN2 dysfunction (*e.g.*, reduced mitochondrial

357 health in general can lead to mitochondrial fragmentation), we also explored other functions performed
358 by MFN2 to provide additional evidence for MFN2 dysfunction.
359
360 **Perturbated Mitochondrial Nucleoids in MFN2 Q367H Patient Fibroblasts**
361 Mitochondria house their own genome, mtDNA, which is present in hundreds of copies
362 throughout the mitochondrial network and is organized into nucleoid structures. As mtDNA nucleoids
363 can be altered by impairments to mitochondrial fusion (37), we sought to examine mtDNA in Q367H
364 patient fibroblasts (Figure 3A/B). Similar to mitochondrial morphology, there were no changes to mtDNA
365 nucleoid size or abundance in standard media. However, under glucose-free galactose-supplemented
366 conditions, patient fibroblasts had a decrease in the average number of mitochondrial nucleoids per cell,
367 while the average nucleoid size was increased (Figure 3A/C). Of note, in both growth conditions, a small
368 number of mtDNA nucleoids were observed outside the mitochondrial network in patient fibroblasts
369 (circled in figure 3A). Meanwhile, the mtDNA copy number did not change under any conditions (Figure
370 3D/E), nor were any mtDNA deletions detected (Figure 3F). Observing fewer, larger nucleoids without
371 changes in mtDNA copy number is likely due to nucleoid clustering, a phenotype often observed with
372 impaired mitochondrial fusion (37). As such, the mtDNA studies are consistent with reduced fusion
373 leading to mitochondrial fragmentation in the Q367H cells when grown in glucose-free galactose-
374 supplemented media.
375
376 **MFN2 Q367H Fibroblasts show reduced number of Mito-ER Contact Sites**
377 MFN2 also mediates mito-ER contact sites (MERCs) (38). As an estimate of MERCs, we used a
378 proximity ligation assay to detect regions where the mitochondria and ER are within ~40 nm. No
379 absolute changes in the number or size of the PLA signals were observed in standard media. However,
380 under glucose-free conditions, Q367H cells had fewer PLA puncta, though these puncta were slightly
381 larger (Figure 4A-C). As changes in MERCs could be due to global changes in mitochondrial abundance,
382 we also measured the area of mitochondria (mitochondrial footprint). Importantly, we do not observe
383 significant differences between mitochondrial footprint in control and patient cells (Figure 4D). However,
384 when the MERC PLA signal is normalized to the mitochondrial footprint, we see a slight a reduction in
385 the number of MERCs in the patient fibroblasts in standard conditions, which is further exaggerated
386 under glucose-free conditions (Figure 4E). Together, these data indicate perturbations in MERCs in the
387 Q367H fibroblasts that are consistent with MFN2 dysfunction.
388

389 **Dysfunction in Mitochondrial Fatty Acid Import Leads to Lipid Droplet Accumulation in Patient**
390 **Fibroblasts**
391 Given the role of MFN2 in mediating mitochondria-lipid droplet interactions, and the fact that
392 lipid droplets are altered in fibroblasts from patients with MFN2 variants (16), we next explored lipid
393 droplets in the Q367H fibroblasts. Interestingly, we see a significant increase in the number and size of
394 cellular lipid droplets in patient fibroblasts, both grown in standard and glucose-free galactose-
395 supplemented media (Figure 5A-D). To explore the mechanism underlying the increased accumulation of
396 lipid droplets, we examined lipid transfer from lipid droplets to mitochondria using an assay that takes
397 advantage of the BODIPY 558/568 fatty acid precursor (39). In this assay, the fluorescently labelled lipid
398 is loaded into lipid droplets during a 24-hour incubation, and its transfer to mitochondria can be
399 monitored over time by microscopy. In control cells in standard conditions, some fatty acid pre-cursor
400 transfers into the mitochondrial network (Figure 5E-F), with higher transfer under glucose starvation
401 conditions (without galactose supplementation). Notably, in patient fibroblasts, no fatty acid trafficking
402 from lipid droplets to mitochondria is observed under either growth condition (Figure 5E-F). These
403 findings suggest that the excess lipid droplets seen in the patient fibroblasts are due to an accumulation
404 of lipids due to a lack of fatty acids transfer from lipid droplets to mitochondria.
405
406 **MFN2 Q367H Patient Cells Show mtDNA-Mediated Inflammation**
407 Following up on observation of nucleoids outside of the mitochondrial network (Fig 3), we
408 looked for evidence of mtDNA-mediated inflammation, which is linked to impaired mitochondrial fusion
409 and can cause myopathy (4). First, to look for signs for an inflammatory response, we examined the
410 expression of several inflammation genes via q-RT-PCR. Notably, even when cells were grown in standard
411 glucose conditions, we observed an elevation of genes that mediate TLR9 signalling (*i.e.*,
412 ASC/NLRP3/S100A9) and downstream cytokines of the TLR9 pathway (*i.e.*, IL6/TNFα), as well as genes
413 downstream of the cGAS-STING pathway (INF-α/β) (Figure 6A). Similar inflammatory signalling was
414 observed when fibroblasts were grown in galactose media (Supplemental Figure 1). To determine if the
415 increased expression of these genes was due to the TLR9 or cGAS-STING signalling pathways, fibroblasts
416 in standard media were treated with chloroquine to inhibit TLR9 signalling (40), or RU.521 (41) to inhibit
417 cGAS (Figure 6A). Strikingly, chloroquine reduced TLR9 targets, while RU.521 reduced cGAS-STING
418 targets. The fact that each treatment significantly reduced expression of the relevant genes to the levels
419 seen in the control patient fibroblasts, confirms that both TLR9-NF-kB and cGAS-STING signalling are
420 elevated in the patient fibroblasts and that these are the primary pathways driving expression.

421 Given the link to TLR9 signalling, which detects mtDNA in endosomes, we also looked to see if
422 mtDNA outside the mitochondrial network colocalized with Rab5C-labelled early endosomes.
423 Remarkably, we observed co-localization of extra-mitochondrial mtDNA with early endosomes, including
424 enlarged endosomes harbouring several mtDNA nucleoids (Figure 6B-C). Overall, these findings point to
425 a mtDNA-mediated sterile inflammatory response, mediated through localization of mtDNA into early
426 endosomes and the cytosol (Figure 6D).
427
428 **MFN2 Q367H Patient Transdifferentiated Myoblasts Show Elevated Inflammation, Disrupted MERCs**
429 **and Reduced mtDNA Nucleoid Content**
430 To examine the cellular and inflammatory phenotypes more closely in a relevant cell type, we
431 transdifferentiated control and patient fibroblasts into myoblasts for additional characterization. Upon
432 transdifferentiating, we still observed increased inflammatory signalling (Figure 7A). However, compared
433 to fibroblast cells, patient myoblasts exhibited an additional 3-fold increase in cGAS-STING interferons,
434 and a 10-fold increase in the TLR9 inflammatory signalling, indicating that these pathways are even more
435 strongly activated in patient muscle cells. Finally, we examined some basic parameters of MFN2
436 functions in our transdifferentiated patient myoblasts. First, we found no changes in gross mitochondrial
437 morphology or the average length of mitochondrial branches in patient myoblasts (Figure 7B-C). Second,
438 patient myoblasts had fewer MERCs, which were also smaller in size (Figure 7D-F). Finally, the mtDNA
439 nucleoid analysis found a reduction in the number nucleoids per cell in patient myoblasts, as well as a
440 decrease in size of the nucleoids (Figure 7G-I). Notably, consistent with findings in patient fibroblasts, a
441 subset of these nucleoids could be found outside of the mitochondrial network.

442 **Discussion:**

443 We report an individual with a late-onset myopathy phenotype and a previously uncharacterized
444 variant in *MFN2*. We pursued the investigations described in this report based on strong clinical
445 suspicion for this as a potential pathogenic variant. This sequence change in *MFN2* replaces glutamine
446 with histidine at codon 367 of the MFN2 protein (Q367H). The glutamine residue is highly conserved,
447 and there is a small physicochemical difference between glutamine and histidine, implying a
448 hypermorphic change. The MFN2 Q367 amino acid is conserved across vertebrate MFN2 sequences, as
449 well as with the MFN1 paralogue (Figure 1D). The MFN2 Q367H variant is present in population
450 databases with a very low allele frequency (highest allele frequency 0.000242 in Gnomad according to
451 dbSNP report rs373211062, accessed June 4, 2024), including one homozygous individual. The variant
452 has an entry in Clinvar (439898, accessed June 4, 2024) and is classified as having conflicting
453 interpretations of pathogenicity, with 4 entries from clinical testing of patients with neurological
454 phenotypes. In a large cohort study, a patient with early onset peripheral neuropathy was reported who
455 was compound heterozygous for Q367H and P184R MFN2 variants (42). However, the
456 Q367H MFN2 variant has not been functionally characterized, or previously reported in the literature as
457 a standalone disease-causing variant. The family history of the patient's parent suggests autosomal
458 dominant inheritance, which is in keeping with this variant, although confirmation of this variant in the
459 parent was not possible. Furthermore, a different amino acid substitution at this position (Q367P) was
460 associated with a neuropathy presentation (43), providing additional support that variants at this
461 position are likely to be associated with this disease. All considered, the Q367H variant is highly plausible
462 as a reduced penetrance pathogenic variant given its extremely low frequency in population databases,
463 its prevalence in individuals with neurological phenotypes, its presence in published cases from
464 literature. The data from studies in this report point to the deleterious nature of the Q367H variant, and
465 importantly demonstrate the damaging effect of this variant in cells transdifferentiated to the muscle
466 lineage.

467 This case illustrates many of the challenges when conducting research with people affected by
468 genetic conditions with very late onset. Information from control population databases may be
469 misleading if individuals are presymptomatic for a very late onset disease, or when phenotypes are very
470 mild and slowly progressive. Even for paediatric-onset disease, pathogenic variants appear in a
471 substantial proportion of control individuals (2.8% in one study)(44) , and this number may be
472 comparable or even higher for very-late onset disorders, such as the one described in this report. Future
473 research will improve our understanding of genetic variants and disorders with very late onset and

474 variable penetrance, but identification and investigation of cases is difficult since they may be mistaken
475 for degenerative or acquired conditions (for example, prior work showing diagnoses of genetic spastic
476 paraplegia in patients initially diagnosed with sporadic primary lateral sclerosis)(45). Other factors
477 include the lack of availability of family members for segregation of variants (i.e: parents have expired by
478 the time the patient is diagnosed, or family members are estranged, or the disease status is not yet
479 known for younger family members). In this respect, we acknowledge limitations of this study which only
480 includes a single affected participant. However, we hope to bring attention to the fact that the
481 investigation of genetic disorders is important to our broader understanding of genetic diseases and
482 operates with the above-mentioned special challenges.

483 Despite the fact that over 150 MFN2 variants have been reported in patients with CMT2A, we
484 still do not have a complete understanding of how MFN2 dysfunction contributes to disease. The
485 rfsituation is complex, as MFN2 has multiple functions in the cell, and CMT2A can have additional
486 pathological phenotypes beyond peripheral neuropathy. Moreover, only a handful of MFN2 variants have
487 been characterized functionally, and even then, often only for one or two of MFN2's known functions
488 (16). Thus, a better understanding of how MFN2 variants affect MFN2 functions is essential to
489 understanding how MFN2 contributes to disease. Here, our characterization of cells from a patient
490 exhibiting distal myopathy who carried the candidate pathogenic MFN2 Q367H variant provides novel
491 mechanistic insight into MFN2-mediated pathology. The fact that several MFN2-mediated functions are
492 impaired in the patient cells, especially when they are forced to use mitochondria for energy production,
493 supports the notion that the Q367H variant impairs MFN2 function and likely contributes to the patient
494 pathology. Moreover, to our knowledge, the association of mtDNA release and inflammation with an
495 MFN2 variant has not been reported previously, and supports a mechanistic pathway by which MFN2
496 dysfunction contributes to inflammation. Finally, the elevated levels of inflammation in patient-derived
497 transdifferentiated myoblasts further support a novel disease pathomechanism for MFN2-mediated
498 inflammation driving myopathy.

499 Several lines of evidence support the pathogenicity of the Q367H MFN2 variant, as patient
500 fibroblasts show perturbation to multiple functions performed by MFN2, including mitochondrial fusion
501 mtDNA nucleoid distribution, MERCs and cellular lipid droplets. With respect to mitochondrial fusion,
502 similar to our findings, several MFN2 variants do not show mitochondrial fragmentation when grown in
503 standard glucose conditions (16). However, culturing fibroblasts in galactose can reveal fragmentation of
504 the mitochondrial network, as reported for MFN2 D210V (9), and as we see for the Q367H variant. This
505 network fragmentation could be caused by reduced fusion and/or increased fission (46). Given the well-

506 defined role of MFN2 in mitochondrial fusion, the fragmentation is consistent with reduced fusion.
507 Meanwhile, as reduced mitochondrial fusion can also impact mtDNA distribution (37), the changes we
508 see in mitochondrial nucleoids are also consistent with reduced fusion in patient fibroblasts when grown
509 in galactose. Taken together, the results are consistent with reduced mitochondrial fusion when cells are
510 grown in galactose.

511 Beyond mitochondrial fusion, perhaps the best characterized function of MFN2 is in regulating
512 MERCs (2). Notably, MERCs in fibroblasts from patients with various *MFN2* variants can show a variety of
513 changes (16), and the reduction in the number and size of MERCs that we observed in patient cells is
514 consistent with MFN2 dysfunction. Intriguingly, altered MERCs could contribute to the patient myopathy,
515 as pathogenic variants in *SEPN1*, another gene implicated in MERC biology, also causes a myopathy
516 phenotype (47).

517 Also consistent with MFN2 dysfunction and in line with our findings, an increased number and
518 size of lipid droplets in fibroblasts is reported in fibroblasts patients with other MFN2 variants (48), as
519 well as upon MFN2 depletion (3). Intriguingly, the lipid droplet phenotype is evident in standard growth
520 conditions when mitochondrial morphology was unaltered. Notably, the mechanism by which impaired
521 MFN2 function leads to increased size and abundance of lipid droplets in patient fibroblasts has not
522 been investigated previously. We envision several possible explanations: decreased transfer of lipids into
523 mitochondria from lipid droplets, or increased transfer of lipids from mitochondria to lipid droplets. Our
524 finding that patient fibroblasts failed to import fatty acids into mitochondria, even under glucose
525 starvation conditions, is in line with the first possibility, and likely reflects the role of MFN2 in mediating
526 mitochondria-lipid droplet interactions (49). Though we expect reduced lipid transfer will also explain
527 the increased lipid droplet accumulation observed in fibroblasts from patients with other MFN2 variants,
528 this remains to be determined.

529 Characterization of the transdifferentiated patient myoblasts provides further evidence of MFN2
530 dysfunction and important insight into the muscle myopathy phenotype in the patient. Consistent with
531 MFN2 dysfunction, we see a significant decrease in the number and size of mitochondrial nucleoids, as
532 well as fewer and smaller MERCs in transdifferentiated patient myoblasts. However, we did not observe
533 any changes in mitochondrial network morphology. Notably, the transdifferentiated myoblasts were
534 grown in standard myoblast media, as opposed to the glucose-free galactose-supplemented media
535 required to elicit differences in the patient fibroblasts. Other differences in growth conditions between
536 transdifferentiated patient myoblasts (*e.g.*, collagen matrix), or the inherent differences between
537 fibroblast and myoblast cell types may also explain differences between patient fibroblasts and

538 transdifferentiated myoblasts. Regardless, the reduced number of nucleoids in the patient cells is
539 consistent with MFN2 dysfunction, as muscle-specific loss of MFN2 leads to mtDNA depletion (17).
540 The finding of mtDNA release and inflammation in both Q367H patient fibroblasts and
541 transdifferentiated myoblasts is novel in the context of pathogenic MFN2 variants and is likely relevant to
542 disease mechanism. The fact that inhibitors of both TLR9/cGAS-STING pathways lead to decrease in their
543 downstream cytokines, indicates that both pathways are activated. These findings are also consistent
544 with previous work on impaired mitochondrial fusion and increased inflammation. With respect to
545 MFNs, a recent paper by Irazoki *et al.*, found that knockdown of either MFN1 or MFN2 in myoblasts
546 could promote TLR9 signalling (4). Arguing that activation of TLR9-mediated inflammation is a general
547 response to loss of mitochondrial fusion, loss of the inner mitochondrial membrane fusion protein OPA1
548 in muscle leads to TLR9-mediated NF-κB activation (but not cGAS-STING), where it also drives an
549 inflammatory myopathy (50). Thus, it seems that loss of fusion is sufficient to induce mtDNA-mediated
550 TLR9 inflammation in muscle cells that can drive myopathy. A mechanism that can explain the phenotype
551 of the patient harbouring the Q367H variant. Meanwhile, the increased cGAS-STING signalling that we
552 also see in Q367H patient cells is consistent with increased cGAS-STING activity also reported in MFN2-
553 deficient myoblasts (4), as well as in microglia where MFN2 is downregulated (51). Whether cGAS-STING
554 signalling further perturbs pathology remains to be determined, though elevated cGAS-STING
555 inflammation is also linked to myopathy (52).
556 Another interesting question involves how MFN2 loss of function drives mtDNA release to
557 stimulate both TLR9 and cGAS-STING inflammation. In this regard, several recent studies are relevant to
558 endosomal-mediated mtDNA release (53–55). A model seems to be emerging where, in the context of
559 stalled mtDNA replication intermediates, enlarged nucleoid clusters are transferred directly into early
560 endosomes, where the mtDNA can be detected by TLR9. When this quality control pathway is
561 overwhelmed, it can lead to release of mtDNA from endosomes into the cytosol, and cGAS-STING
562 activation (54). Notably, one mechanism by which loss of mitochondrial fusion is proposed to impact the
563 mtDNA is through imbalanced distribution of mtDNA maintenance proteins (56), which may lead to an
564 increased abundance of stalled mtDNA replication intermediates. Thus, mtDNA replication fork stalling in
565 response to impaired mitochondrial fusion may trigger initial mtDNA release into endosomes, and the
566 subsequent TLR9 activation associated with MFN2 dysfunction. The fact that we see extra mtDNA and
567 inflammatory signalling in patient cells with normal mitochondrial morphology (*e.g.*, fibroblasts grown in
568 standard media, and differentiated myoblasts), suggests that even subtle alterations in mitochondrial
569 fusion are sufficient to impact the mtDNA. Alternatively (or in conjunction), the differences in MERCs,

570 which can demarcate sites of mtDNA replication (57,58), could also impair mtDNA replication and trigger
571 to mtDNA release into endosomes.
572 Meanwhile, as elevated cGAS-STING is not found with MFN1 or OPA1 depletion (4,50,59), the
573 elevated cGAS-STING signalling in myoblasts devoid of MFN2 (4), and seen here in MFN2 Q367H patient
574 cells, suggests another role for MFN2 in mediating mtDNA release beyond just reduced mitochondrial
575 fusion. In this regard, MFN2 can interact with RAB5C on early endosomes (4). As such, it is tempting to
576 speculate that MFN2 has a role in mediating the mitochondrial-endosome interactions required for
577 endosome-mediated removal of stalled mtDNA replication intermediates, and that disrupting this
578 interaction promotes mtDNA escape into the cytosol to activate cGAS-STING inflammation. Future
579 studies examining the mechanisms of mtDNA release will likely provide more insight to the role played
580 by MFN2 and may benefit from examining the Q367H variant as a means to perturb MFN2 function.
581 It is worth noting that MFN2 could also influence inflammation through its other functions. For
582 example, there are connections between disrupted MERCs and activation of sterile inflammation,
583 particularly in high energy-demanding tissues such as the heart (60). Meanwhile, relevant to the
584 increased lipid droplet abundance associated with MFN2 dysfunction and seen even in standard growth
585 conditions with normal mitochondrial morphology, it is notable that lipid droplet biology intersects with
586 inflammation. Specifically, elevated lipid droplet abundance correlates with increased inflammation (61–
587 64). Overall, our findings are consistent with MFN2 dysfunction contributing to inflammation, which is a
588 possible explanation for myopathy initially described in the proband.
589 The patient presentation, with late onset myopathy, but without neuropathy, offers a unique
590 opportunity to separate the pathological outcomes of MFN2 dysfunction by examining the specific
591 mechanism leading to myopathy. Although myopathy has been reported previously in patients with
592 CMT2A (10,11), it has always been in the context of a peripheral neuropathy where it is generally
593 considered to be a downstream consequence of nerve loss. For example, the MFN2 D210V variant has
594 myopathy phenotypes in a three-generational case study, which has accompanying axonal neuropathy
595 (9). On the other hand, arguing against the notion of muscle loss downstream of neuropathy,
596 mitochondrial myopathy is seen in a skeletal muscle-specific MFN2 loss-of-function study in animal
597 models, highlighting the importance of the protein in tissues such as skeletal muscle (65,66). Meanwhile,
598 in cardiac muscle, the MFN2 R400Q variant is implicated in cardiomyopathy, though no link to
599 inflammation was investigated (67). Additionally, the loss of MFN2 protein expression in skeletal muscles
600 correlates with age and could contribute to sarcopenia through a similar inflammatory mechanism (68).
601 Finally, similar to the patient we describe here, a novel ENU-induced Mfn2 mouse model characterized

602 L643P as a variant that causes muscle myopathy without peripheral neuropathy (69). Together, these
603 findings show that MFN2 dysfunction can cause muscle myopathy in the absence of nerve degeneration,
604 as observed in the proband.

605 With respect to how MFN2 dysfunction might cause myopathy, in the first report of an MFN2-
606 specific mouse muscle knockout, the authors argued that the mtDNA depletion was likely a key
607 contributory factor due to reduced oxidative phosphorylation (65). However, more recent work linking
608 MFN1 and OPA1 muscle deficiency to inflammation mediated myopathy, showed that blocking the
609 inflammation was protective in these models (4,50), arguing for a key role of inflammation in the muscle
610 pathology caused by impaired mitochondrial fusion. Mechanistically, inflammation in the muscle cell
611 niche can lead to myopathy and interfere with muscle stem cell populations (70), as well as affect the
612 expression of myogenic genes (71). Meanwhile, NF-kB, a proinflammatory cytokine that is downstream
613 of TLR9 signaling, can cause muscle wasting in mice (72). Building on these findings, it is tempting to
614 speculate that mtDNA-mediated inflammation may also be relevant to idiopathic inflammatory
615 myopathies, a heterogeneous group of autoimmune disorders with varying clinical manifestations,
616 primarily defined by muscle weakness (73,74). In this regard, we speculate that the mtDNA-mediated
617 inflammation discovered in Q367H patient-derived cells is contributing to the patient's myopathy.

618 Although MFN1 and OPA1 deficiency can cause inflammatory myopathy in mouse muscle
619 knockout models, the role of mtDNA-mediated inflammation in MFN2 pathology has not been fully
620 explored. While a mouse knock-in model of the MFN2 K357T variant is linked to augmented
621 neuroinflammation in response to LPS treatment, the role of mtDNA was not investigated (75). Our
622 findings linking the MFN2 Q367H variant to mtDNA release and inflammation thus provide a novel
623 disease mechanism for MFN2 dysfunction. Moreover, while our findings are relevant to the myopathy
624 phenotype in muscle, it is also possible that mtDNA-mediated inflammation contributes to the
625 peripheral neuropathy in neurons. Intriguingly, peripheral neuropathy is a common phenotype of several
626 DNA damaging agents (76–80) , such as doxorubicin, which can damage mtDNA and lead to mtDNA-
627 mediated cGAS-STING inflammation (81).

628 In summary, we observed elevated mtDNA-mediated TLR9/NF-kB and cGAS-STING inflammatory
629 signaling in a patient harboring the uncharacterized MFN2 Q367H variant who displayed late-onset
630 myopathy as a standalone phenotype. Moreover, functional analyses of patient fibroblasts provided
631 several lines of evidence consistent with MFN2 dysfunction. Critically, characterization of
632 transdifferentiated myoblasts and the elucidation of a novel link to mtDNA-mediated inflammation may
633 mechanistically explain the myopathy phenotype in the patient.

Acknowledgements

The authors would like to thank the study participants and their family. Lentivirus production was performed by the Hotchkiss Brain Institute Molecular Core Facility at the University of Calgary.

Author contributions

Designed and/or performed and analyzed mitochondrial experiments, MZ, GS, WA, TS, MJ, RS, GP, and TES; Clinical evaluation of patients, GP; Analyzed exome data GP, MJ,; Performed skin biopsy from mitochondrial patients, GP; Drafted the manuscript or figures, MZ, GP, TES. All authors discussed the results and commented on the manuscript. GS, and WA are joint second authors. TES and GP are co-corresponding authors.

Funding

This work was supported by funds provided by the Alberta Children's Hospital Research Institute (TES), the Canadian Institutes of Health Research (TES), and the New Frontiers Research Fund (TES). MZ was supported by a Hotchkiss Brain Institute International Recruitment Scholarship. WA was supported by the Saudi Cultural Bureau. R.S. was supported by a QEII Graduate Scholarship. TGBS was supported by an Alberta Graduate Excellence Scholarship and a University of Calgary Faculty of Graduate Studies Doctoral Scholarship. MJ is the recipient of the Katharine Sarah Melinda Mei-Ling Thomas Rare Diseases Scholarship. Infrastructure in the lab of GP for this work was supported by the HBI Dementia Research Equipment Fund and a Canada Foundation for Innovation JELF Grant (Neuromuscular Genetics, 36624). The funders had no role in study design, data collection and interpretation, or the decision to submit the work for publication.

657 **Figure Legends:**

658 **Figure 1: Initial characterization of patient phenotypes and MFN2 Q367H variant.**

659 A. MRI image at the level of the legs demonstrating predominant atrophy in white arrows;
660 Gastrocnemius (A) , Soleus (B) and Tibialis Anterior (C) bilaterally. B. MRI image of upper Thighs
661 demonstrating predominant atrophy of adductor longus gluteus minimus (Non shown here).
662 C.(i) Sanger sequencing results showing single nucleotide polymorphism in patient fibroblasts, transition
663 Guanine to Cytosine. (ii) Topology diagram of MFN2 protein with domains and localization indicated. The
664 site of the Q367H variant is shown in the diagram. D. Amino acid sequence alignment using T-COFFEE
665 tool. E. Western Blot analysis comparing expression of mitochondrial fusion protein in control vs patient
666 fibroblasts, normalized to β-actin. (F-J) Comparison of protein expression levels (F) MFN2 (glucose
667 media) (G) MFN2 (glucose-free/galactose supplemented media) (H) MFN1 (I) OPA1 levels in control vs
668 patient fibroblasts. Data is indicative of mean +/- SD. Statistical comparisons were made by unpaired t-
669 test, (ns=not significant ($p>0.05$)).

670

671 **Figure 2: Changes in mitochondrial morphology and respiratory function.**

672 (A) Representative confocal images (top) with zoomed inset images (bottom) showing mitochondrial
673 network morphology in control vs patient fibroblasts stained with TOMM20. (B) Qualitative scoring of
674 proportion of cells showing fragmented/intermediate/fused mitochondrial network. Bars indicate mean
675 +/-SD. (C) Quantitative analysis of mean mitochondrial branch length in control vs patient fibroblasts
676 using glucose or glucose-free/galactose supplemented media, bars show mean +/- SD, colours indicate
677 biological replicates. (D) Oxygen Consumption Rate (OCR) assay on control and patient fibroblasts using
678 Seahorse XFe24, bars indicate mean +/- SD (n=12 replicates). Statistical comparisons were made by
679 unpaired t-test (ns=not significant ($p>0.05$); ****=$p\leq 0.0001$).

680

681 **Figure 3: Characterization of mtDNA nucleoids, mtDNA copy number, and mtDNA deletions.**

682 (A) Representative confocal images showing mitochondria (TOMM20; grey) and mitochondrial nucleoids
683 (dsDNA antibody; red) in patient and control fibroblasts under glucose and glucose-free/galactose
684 supplemented nutrient conditions. Circles indicate presence of mtDNA nucleoids outside the
685 mitochondrial network. (B) Number of nucleoids per cell, mean is shown with colours indicating
686 biological replicates. (C) Average size of mitochondrial nucleoids, violin plots show median and
687 interquartile ranges. (D-E) qPCR data showing mitochondrial DNA copy number in (D) glucose and (E)
688 glucose-free/galactose supplemented media, bars indicate mean +/- SD. (F) Agarose gel electrophoresis

689 showing long range PCR products used to detect full-length or deleted mtDNA and DNA ladder showing
690 corresponding sizes. Statistical comparisons were made by unpaired t-test, (ns=not significant ($p>0.05$);
691 *=$p\leq 0.05$; ***=$p\leq 0.001$; ****=$p\leq 0.0001$).
692
693
694 **Figure 4: Mito-ER Contact site alterations.**
695 (A) Representative confocal images of mito-ER contact sites (MERCs) using proximity ligation assay (PLA)
696 showing mitochondria (TOMM20; cyan), PLA probes (green) and ER (Calnexin; magenta) in glucose and
697 glucose-free/galactose supplemented media. (B) Quantitative analysis of number of MERCs per cell, lines
698 indicate mean +/- SD, colours indicate biological replicates. (C) Quantitative analysis of average size of
699 PLA probes, with violin plots indicate median and interquartile range. (D) Quantitative analysis of
700 mitochondrial area in each cell type in (μm^2), lines show mean +/- SD, colours indicate biological
701 replicates. (E) Normalized number of MERCs to total mitochondrial area per cell, lines indicate mean +/-
702 SD, colours indicate biological replicates. P-values determined by unpaired t-test (ns=not significant
703 ($p>0.05$); *=$p\leq 0.05$; **=$p\leq 0.01$; ****=$p\leq 0.0001$).
704
705 **Figure 5: Changes to cellular lipid droplets.**
706 (A-B) Representative confocal images showing lipid droplets stained with HCS LipidTox Green in (A)
707 glucose and (B) glucose-free/galactose supplemented media. (C) Quantitative analysis of the average
708 number of lipid droplets per cell, bars indicate mean +/- SD, colours indicate biological replicates. (D)
709 Quantitative analysis of the average size of lipid droplets, violin plots show median and interquartile
710 range. (E) Representative live-cell confocal images showing mitochondria (MitoTracker Green) and fatty
711 acids (BODIPY 558/568) at 0 hours and 24 hours in standard or glucose-starved media. (F) Quantitative
712 analysis of co-localization between fatty acid and mitochondrial network, colours indicate cell type (red-
713 control and blue-MFN2 Q367H), bars indicate mean +/- SD. P-values determined by unpaired t-test
714 (ns=not significant ($p>0.05$); **=$p\leq 0.01$; ****=$p\leq 0.0001$).
715
716 **Figure 6: MFN2 Q367H cells show activation of TLR9 and cGAS-STING inflammatory pathways, and co-**
717 **localization of mtDNA with early endosomes.**
718 (A) RT-qPCR data showing gene expression for TLR9/NF-KB targets (Asc, IL6, NLRP3, S100a9, TNF) and
719 cGAS-STING targets (Ifn-α, Ifn-β) in control vs patient fibroblasts under glucose conditions. The graph
720 also shows the effects of inhibitors for the TLR pathway (Chloroquine) or cGAS-STING pathway (RU.521).

721 Lines indicate mean +/- SD. (B) Representative confocal images showing mitochondria (TOMM20; cyan),
722 mitochondrial nucleoids (anti-dsDNA antibody; green), and early endosomes (RAB5C;magenta). Images
723 in inset bottom right panel highlights the location of mitochondrial nucleoids outside the mitochondria
724 with the early endosomes, denoted by the white arrows. (C) Quantitative analysis of signal co-
725 localization between mitochondrial nucleoids and early endosomes in patient and control fibroblasts
726 determined by Pearson's coefficient, lines indicate mean +/- SD, points indicate replicates. (D) Pathway
727 model representing mitochondrial dysfunction leading to sterile inflammation. The diagram shows how
728 the MFN2 Q367H variant can alter mitochondrial function, leading to transfer of mtDNA from the
729 mitochondria to the early endosomes (middle). This can lead to detection by TLR9 and subsequent
730 activation of the NF-kB mediated inflammation (right). Additionally, mtDNA in the early endosomes
731 could leak into the cytosol, leading to detection through the cGAS-STING pathway (middle-bottom),
732 promoting Type-I Interferon mediated inflammation (right). Collectively, the inflammation contributes to
733 the distal myopathy disease outcome in the patient. P-values determined by unpaired t-test (ns=not
734 significant ($p>0.05$); *=$p\leq 0.05$; ****=$p\leq 0.0001$).
735
736
737 **Figure 7: Altered MFN2 functions in transdifferentiated patient myoblasts.**
738 (A) RT-qPCR data showing gene expression for TLR9/NF-KB targets (Asc, IL6, NLRP3, S100a9, TNF) and
739 cGAS-STING targets (Ifn-α, Ifn-β) in control vs patient myoblasts, lines indicate mean +/- SD.(B)
740 Representative confocal images showing mitochondrial network morphology (TOMM20; cyan) in control
741 and patient myoblasts. (C) Quantitative analysis of mean mitochondrial branch length in control and
742 patient myoblasts, violin plots show median and interquartile ranges. (D) Representative confocal images
743 of control and patient myoblasts showing PLA probes (representing MERCs; green), mitochondria
744 (TOMM20; cyan) and ER (Calnexin; magenta). (E) Quantitative analysis of the number of MERCs per cell
745 in control and patient myoblasts, violin plots show media and interquartile ranges. (F) Quantitative
746 analysis of average size of MERCs per cell in control and patient myoblasts, violin plots show media and
747 interquartile ranges. (G) Representative confocal images showing mitochondria (TOMM20) and
748 mitochondrial nucleoids (dsDNA antibody). Circles indicate mtDNA staining outside the mitochondrial
749 network. (H) Quantification of average number of nucleoids per cell in control and patient myoblasts,
750 violin plots show median and interquartile ranges. (I) Quantification of average size of mtDNA nucleoids
751 in control and patient myoblasts. Violin plots show median and interquartile ranges. P-values
752 determined by unpaired t-test (ns=not significant ($p>0.05$); ***=$p\leq 0.001$; ****=$p\leq 0.0001$).

753 **References**

754 1. Filadi R, Pendin D, Pizzo P. Mitofusin 2: from functions to disease. Cell Death Dis. 2018 Feb
755 28;9(3):330.

756 2. de Brito OM, Scorrano L. Mitofusin 2 tethers endoplasmic reticulum to mitochondria. Nature.
757 2008 Dec 4;456(7222):605–10.

758 3. Boutant M, Kulkarni SS, Joffraud M, Ratajczak J, Valera-Alberni M, Combe R, et al. Mfn2 is critical
759 for brown adipose tissue thermogenic function. EMBO J. 2017 Jun 1;36(11):1543–58.

760 4. Irazoki A, Gordaliza-Alaguero I, Frank E, Giakoumakis NN, Seco J, Palacín M, et al. Disruption of
761 mitochondrial dynamics triggers muscle inflammation through interorganellar contacts and
762 mitochondrial DNA mislocation. Nat Commun. 2023 Jan 6;14(1):108.

763 5. Zervopoulos SD, Boukouris AE, Saleme B, Haromy A, Tejay S, Sutendra G, et al. MFN2-driven
764 mitochondria-to-nucleus tethering allows a non-canonical nuclear entry pathway of the mitochondrial
765 pyruvate dehydrogenase complex. Mol Cell. 2022 Mar 3;82(5):1066-1077.e7.

766 6. Li J, Dang X, Franco A, Dorn GW. Reciprocal Regulation of Mitofusin 2-Mediated Mitophagy and
767 Mitochondrial Fusion by Different PINK1 Phosphorylation Events. Front Cell Dev Biol. 2022;10:868465.

768 7. McLelland GL, Goiran T, Yi W, Dorval G, Chen CX, Lauinger ND, et al. Mfn2 ubiquitination by
769 PINK1/parkin gates the p97-dependent release of ER from mitochondria to drive mitophagy. Dikic I,
770 editor. eLife. 2018 Apr 20;7:e32866.

771 8. Feely SME, Laura M, Siskind CE, Sottile S, Davis M, Gibbons VS, et al. MFN2 mutations cause
772 severe phenotypes in most patients with CMT2A. Neurology. 2011 May 17;76(20):1690–6.

773 9. Rouzier C, Bannwarth S, Chaussenot A, Chevrollier A, Verschueren A, Bonello-Palot N, et al. The
774 MFN2 gene is responsible for mitochondrial DNA instability and optic atrophy “plus” phenotype. Brain J
775 Neurol. 2012 Jan;135(Pt 1):23–34.

776 10. Abati E, Manini A, Velardo D, Del Bo R, Napoli L, Rizzo F, et al. Clinical and genetic features of a
777 cohort of patients with MFN2-related neuropathy. Sci Rep. 2022 Apr 13;12(1):6181.

778 11. Verhoeven K, Claeys KG, Züchner S, Schröder JM, Weis J, Ceuterick C, et al. MFN2 mutation
779 distribution and genotype/phenotype correlation in Charcot–Marie–Tooth type 2. Brain. 2006 Aug
780 1;129(8):2093–102.

781 12. Sharma G, Zaman M, Sabouny R, Joel M, Martens K, Martino D, et al. Characterization of a novel
782 variant in the HR1 domain of MFN2 in a patient with ataxia, optic atrophy and sensorineural hearing loss.
783 F1000Research. 2022 Sep 2;10:606.

784 13. Sawyer SL, Cheuk-Him Ng A, Innes AM, Wagner JD, Dyment DA, Tetreault M, et al. Homozygous
785 mutations in MFN2 cause multiple symmetric lipomatosis associated with neuropathy. Hum Mol Genet.
786 2015 Sep 15;24(18):5109–14.

787 14. Mann JP, Duan X, Patel S, Tábara LC, Scurria F, Alvarez-Guaita A, et al. A mouse model of human
788 mitofusin-2-related lipodystrophy exhibits adipose-specific mitochondrial stress and reduced leptin
789 secretion. eLife. 2023 Feb 1;12:e82283.

790 15. Masingue M, Vatier C, Jéru I, Latour P, Jardel C, Laforêt P, et al. Homozygous p.R707W MFN2
791 mutation is associated with neuropathy, lipomatosis, peripheral lipoatrophy and metabolic alterations.
792 Neuromuscul Disord. 2017 Oct 1;27:S148.

793 16. Zaman M, Shutt TE. The Role of Impaired Mitochondrial Dynamics in MFN2-Mediated Pathology.
794 Front Cell Dev Biol. 2022;10:858286.

795 17. Chen H, Vermulst M, Wang YE, Chomyn A, Prolla TA, McCaffery JM, et al. Mitochondrial fusion is
796 required for mtDNA stability in skeletal muscle and tolerance of mtDNA mutations. Cell. 2010 Apr
797 16;141(2):280–9.

798 18. Rodríguez-Nuevo A, Díaz-Ramos A, Noguera E, Díaz-Sáez F, Duran X, Muñoz JP, et al.
799 Mitochondrial DNA and TLR9 drive muscle inflammation upon Opa1 deficiency. EMBO J. 2018 May
800 15;37(10):e96553.

801 19. Sidarala V, Zhu J, Levi-D'Ancona E, Pearson GL, Reck EC, Walker EM, et al. Mitofusin 1 and 2
802 regulation of mitochondrial DNA content is a critical determinant of glucose homeostasis. Nat Commun.
803 2022 Apr 29;13(1):2340.

804 20. Vielhaber S, Debska-Vielhaber G, Peeva V, Schoeler S, Kudin AP, Minin I, et al. Mitofusin 2
805 mutations affect mitochondrial function by mitochondrial DNA depletion. Acta Neuropathol (Berl). 2013
806 Feb;125(2):245–56.

807 21. Al Khatib I, Deng J, Lei Y, Torres-Odio S, Rojas GR, Newman LE, et al. Activation of the cGAS-STING
808 innate immune response in cells with deficient mitochondrial topoisomerase TOP1MT. Hum Mol Genet.
809 2023 Jul 20;32(15):2422–40.

810 22. Kim J, Kim HS, Chung JH. Molecular mechanisms of mitochondrial DNA release and activation of
811 the cGAS-STING pathway. Exp Mol Med. 2023 Mar;55(3):510–9.

812 23. Pereira CA, Carlos D, Ferreira NS, Silva JF, Zanotto CZ, Zamboni DS, et al. Mitochondrial DNA
813 Promotes NLRP3 Inflammasome Activation and Contributes to Endothelial Dysfunction and Inflammation
814 in Type 1 Diabetes. Front Physiol. 2019;10:1557.

815 24. Qiu Y, Huang Y, Chen M, Yang Y, Li X, Zhang W. Mitochondrial DNA in NLRP3 inflammasome
816 activation. Int Immunopharmacol. 2022 Jul;108:108719.

817 25. Martens K, Leckie J, Fok D, Wells RA, Chhibber S, Pfeffer G. Case Report: Calpainopathy
818 Presenting After Bone Marrow Transplantation, With Studies of Donor Genetic Content in Various Tissue
819 Types. Front Neurol. 2020;11:604547.

820 26. Griffin HR, Pyle A, Blakely EL, Alston CL, Duff J, Hudson G, et al. Accurate mitochondrial DNA
821 sequencing using off-target reads provides a single test to identify pathogenic point mutations. Genet
822 Med. 2014 Dec;16(12):962–71.

823 27. Di Tommaso P, Moretti S, Xenarios I, Orobitg M, Montanyola A, Chang JM, et al. T-Coffee: a web
824 server for the multiple sequence alignment of protein and RNA sequences using structural information
825 and homology extension. Nucleic Acids Res. 2011 Jul;39(Web Server issue):W13-17.

826 28. UniProt Consortium. UniProt: the Universal Protein Knowledgebase in 2023. Nucleic Acids Res.
827 2023 Jan 6;51(D1):D523–31.

828 29. Schindelin J, Arganda-Carreras I, Frise E, Kaynig V, Longair M, Pietzsch T, et al. Fiji: an open-
829 source platform for biological-image analysis. Nat Methods. 2012 Jun 28;9(7):676–82.

830 30. Uddin GM, Lacroix R, Zaman M, Khatib IA, Rho JM, Kurrasch DM, et al. The Ketogenic Diet
831 Metabolite β-Hydroxybutyrate Promotes Mitochondrial Elongation via Deacetylation and Improves
832 Autism-like Behavior in Zebrafish. bioRxiv. 2022 Jan 1;2022.10.03.510695.

833 31. Zhao T, Goedhart CM, Sam PN, Sabouny R, Lingrell S, Cornish AJ, et al. PISD is a mitochondrial
834 disease gene causing skeletal dysplasia, cataracts, and white matter changes. Life Sci Alliance. 2019
835 Apr;2(2):e201900353.

836 32. Al Khatib I, Deng J, Symes A, Kerr M, Zhang H, Huang SYN, et al. Functional characterization of
837 two variants of mitochondrial topoisomerase TOP1MT that impact regulation of the mitochondrial
838 genome. J Biol Chem. 2022 Oct;298(10):102420.

839 33. Valente AJ, Maddalena LA, Robb EL, Moradi F, Stuart JA. A simple ImageJ macro tool for
840 analyzing mitochondrial network morphology in mammalian cell culture. Acta Histochem. 2017
841 Apr;119(3):315–26.

842 34. Bolte S, Cordelières FP. A guided tour into subcellular colocalization analysis in light microscopy. J
843 Microsc. 2006 Dec;224(Pt 3):213–32.

844 35. Zhang Q, Bethmann C, Worth NF, Davies JD, Wasner C, Feuer A, et al. Nesprin-1 and -2 are
845 involved in the pathogenesis of Emery Dreifuss muscular dystrophy and are critical for nuclear envelope
846 integrity. Hum Mol Genet. 2007 Dec 1;16(23):2816–33.

847 36. Beręsewicz M, Boratyńska-Jasińska A, Charzewski Ł, Kawalec M, Kabzińska D, Kochański A, et al.
848 The Effect of a Novel c.820C>T (Arg274Trp) Mutation in the Mitofusin 2 Gene on Fibroblast Metabolism
849 and Clinical Manifestation in a Patient. PloS One. 2017;12(1):e0169999.

850 37. Sabouny R, Shutt TE. The role of mitochondrial dynamics in mtDNA maintenance. J Cell Sci. 2021
851 Dec 15;134(24):jcs258944.

852 38. de Brito OM, Scorrano L. Mitofusin 2 tethers endoplasmic reticulum to mitochondria. Nature.
853 2008 Dec 4;456(7222):605–10.

854 39. Rambold AS, Cohen S, Lippincott-Schwartz J. Fatty acid trafficking in starved cells: regulation by
855 lipid droplet lipolysis, autophagy, and mitochondrial fusion dynamics. Dev Cell. 2015 Mar 23;32(6):678–
856 92.

857 40. Yasuda H, Leelahavanichkul A, Tsunoda S, Dear JW, Takahashi Y, Ito S, et al. Chloroquine and
858 inhibition of Toll-like receptor 9 protect from sepsis-induced acute kidney injury. Am J Physiol Renal
859 Physiol. 2008 May;294(5):F1050–8.

860 41. Vincent J, Adura C, Gao P, Luz A, Lama L, Asano Y, et al. Small molecule inhibition of cGAS
861 reduces interferon expression in primary macrophages from autoimmune mice. Nat Commun. 2017 Sep
862 29;8(1):750.

863 42. Pipis M, Feely SME, Polke JM, Skorupinska M, Perez L, Shy RR, et al. Natural history of Charcot-
864 Marie-Tooth disease type 2A: a large international multicentre study. Brain J Neurol. 2020 Dec
865 1;143(12):3589–602.

866 43. Xie Y, Li X, Liu L, Hu Z, Huang S, Zhan Y, et al. MFN2-related genetic and clinical features in a
867 cohort of Chinese CMT2 patients. J Peripher Nerv Syst JPNS. 2016 Mar;21(1):38–44.

868 44. Tarailo-Graovac M, Zhu JYA, Matthews A, van Karnebeek CDM, Wasserman WW. Assessment of
869 the ExAC data set for the presence of individuals with pathogenic genotypes implicated in severe
870 Mendelian pediatric disorders. Genet Med Off J Am Coll Med Genet. 2017 Dec;19(12):1300–8.

871 45. Almomen M, Martens K, Quadir A, Pontifex CS, Hanson A, Korngut L, et al. High diagnostic yield
872 and novel variants in very late-onset spasticity. J Neurogenet. 2019 Mar;33(1):27–32.

873 46. Sharma G, Pfeffer G, Shutt TE. Genetic Neuropathy Due to Impairments in Mitochondrial
874 Dynamics. Biology. 2021 Apr;10(4):268.

875 47. Filipe A, Chernorudskiy A, Arbogast S, Varone E, Villar-Quiles RN, Pozzer D, et al. Defective
876 endoplasmic reticulum-mitochondria contacts and bioenergetics in SEPN1-related myopathy. Cell Death
877 Differ. 2021 Jan;28(1):123.

878 48. Larrea D, Pera M, Gonnelli A, Quintana-Cabrera R, Akman HO, Guardia-Laguarta C, et al. MFN2
879 mutations in Charcot-Marie-Tooth disease alter mitochondria-associated ER membrane function but do
880 not impair bioenergetics. Hum Mol Genet. 2019 Jun 1;28(11):1782–800.

881 49. Boutant M, Kulkarni SS, Joffraud M, Ratajczak J, Valera-Alberni M, Combe R, et al. Mfn2 is critical
882 for brown adipose tissue thermogenic function. EMBO J. 2017 Jun 1;36(11):1543–58.

883 50. Rodríguez-Nuevo A, Díaz-Ramos A, Noguera E, Díaz-Sáez F, Duran X, Muñoz JP, et al.
884 Mitochondrial DNA and TLR9 drive muscle inflammation upon Opa1 deficiency. EMBO J. 2018 May
885 15;37(10):e96553.

886 51. Wei FL, Wang TF, Wang CL, Zhang ZP, Zhao JW, Heng W, et al. Cytoplasmic Escape of
887 Mitochondrial DNA Mediated by Mfn2 Downregulation Promotes Microglial Activation via cGas-Sting
888 Axis in Spinal Cord Injury. Adv Sci Weinh Baden-Wurtt Ger. 2023 Nov 27;e2305442.

889 52. Zhou M, Cheng X, Zhu W, Jiang J, Zhu S, Wu X, et al. Activation of cGAS-STING pathway - A
890 possible cause of myofiber atrophy/necrosis in dermatomyositis and immune-mediated necrotizing
891 myopathy. J Clin Lab Anal. 2022 Oct;36(10):e24631.

892 53. Sen A, Boix J, Pla-Martín D. Endosomal-dependent mitophagy coordinates mitochondrial
893 nucleoid and mtDNA elimination. Autophagy. 19(9):2609–10.

894 54. Newman LE, Tadepalle N, Novak SW, Schiavon CR, Rojas GR, Chevez JA, et al. Endosomal removal
895 and disposal of dysfunctional, immunostimulatory mitochondrial DNA [Internet]. Cell Biology; 2022 Oct
896 [cited 2024 Feb 19]. Available from: http://biorxiv.org/lookup/doi/10.1101/2022.10.12.511955

897 55. Sen A, Kallabis S, Gaedke F, Jüngst C, Boix J, Nüchel J, et al. Mitochondrial membrane proteins
898 and VPS35 orchestrate selective removal of mtDNA. Nat Commun. 2022 Nov 7;13:6704.

899 56. Silva Ramos E, Motori E, Brüser C, Kühl I, Yeroslaviz A, Ruzzenente B, et al. Mitochondrial fusion
900 is required for regulation of mitochondrial DNA replication. PLoS Genet. 2019 Jun;15(6):e1008085.

901 57. Ilamathi HS, Benhammouda S, Lounas A, Al-Naemi K, Desrochers-Goyette J, Lines MA, et al.
902 Contact sites between endoplasmic reticulum sheets and mitochondria regulate mitochondrial DNA
903 replication and segregation. iScience. 2023 Jul 21;26(7):107180.

904 58. Lewis SC, Uchiyama LF, Nunnari J. ER-mitochondria contacts couple mtDNA synthesis with
905 mitochondrial division in human cells. Science. 2016 Jul 15;353(6296):aaf5549.

906 59. Tur J, Pereira-Lopes S, Vico T, Marín EA, Muñoz JP, Hernández-Alvarez M, et al. Mitofusin 2 in
907 Macrophages Links Mitochondrial ROS Production, Cytokine Release, Phagocytosis, Autophagy, and
908 Bactericidal Activity. Cell Rep. 2020 Aug 25;32(8):108079.

909 60. Liu H, Liu X, Zhuang H, Fan H, Zhu D, Xu Y, et al. Mitochondrial Contact Sites in Inflammation-
910 Induced Cardiovascular Disease. Front Cell Dev Biol. 2020 Jul 30;8:692.

911 61. Akhmetova K, Balasov M, Chesnokov I. Drosophila STING protein has a role in lipid metabolism.
912 eLife. 2021 Sep 1;10:e67358.

913 62. Bai J, Cervantes C, He S, He J, Plasko GR, Wen J, et al. Mitochondrial stress-activated cGAS-STING
914 pathway inhibits thermogenic program and contributes to overnutrition-induced obesity in mice.
915 Commun Biol. 2020 May 22;3(1):257.

916 63. Monson EA, Crosse KM, Das M, Helbig KJ. Lipid droplet density alters the early innate immune
917 response to viral infection. Zhang L, editor. PLOS ONE. 2018 Jan 2;13(1):e0190597.

918 64. Boucher DM, Vijithakumar V, Ouimet M. Lipid Droplets as Regulators of Metabolism and
919 Immunity. Immunometabolism [Internet]. 2021 Jul [cited 2024 Feb 19];3(3). Available from:
920 https://journals.lww.com/10.20900/immunometab20210021

921 65. Chen H, Vermulst M, Wang YE, Chomyn A, Prolla TA, McCaffery JM, et al. Mitochondrial fusion is
922 required for mtDNA stability in skeletal muscle and tolerance of mtDNA mutations. Cell. 2010 Apr
923 16;141(2):280–9.

924 66. Chen Z, Bordieanu B, Kesavan R, Lesner NP, Venigalla SSK, Shelton SD, et al. Lactate metabolism
925 is essential in early-onset mitochondrial myopathy. Sci Adv. 2023 Jan 4;9(1):eadd3216.

926 67. Franco A, Li J, Kelly DP, Hershberger RE, Marian AJ, Lewis RM, et al. A human mitofusin 2
927 mutation can cause mitophagic cardiomyopathy. eLife. 2023 Nov 1;12:e84235.

928 68. Sebastián D, Sorianello E, Segalés J, Irazoki A, Ruiz-Bonilla V, Sala D, et al. Mfn2 deficiency links
929 age-related sarcopenia and impaired autophagy to activation of an adaptive mitophagy pathway. EMBO
930 J. 2016 Aug 1;35(15):1677–93.

931 69. Hines TJ, Bailey J, Liu H, Guntur AR, Seburn KL, Pratt SL, et al. A Novel ENU-Induced Mfn2
932 Mutation Causes Motor Deficits in Mice without Causing Peripheral Neuropathy. Biology. 2023 Jul
933 3;12(7):953.

934 70. Perandini LA, Chimin P, Lutkemeyer D da S, Câmara NOS. Chronic inflammation in skeletal muscle
935 impairs satellite cells function during regeneration: can physical exercise restore the satellite cell niche?
936 FEBS J. 2018 Jun;285(11):1973–84.

937 71. Chandran R, Knobloch TJ, Anghelina M, Agarwal S. Biomechanical signals upregulate myogenic
938 gene induction in the presence or absence of inflammation. Am J Physiol Cell Physiol. 2007
939 Jul;293(1):C267-276.

940 72. Cai D, Frantz JD, Tawa NE, Melendez PA, Oh BC, Lidov HGW, et al. IKKbeta/NF-kappaB activation
941 causes severe muscle wasting in mice. Cell. 2004 Oct 15;119(2):285–98.

942 73. Lundberg IE, Fujimoto M, Vencovsky J, Aggarwal R, Holmqvist M, Christopher-Stine L, et al.
943 Idiopathic inflammatory myopathies. Nat Rev Dis Primer. 2021 Dec 2;7(1):86.

944 74. Silva AMS, Campos ED, Zanoteli E. Inflammatory myopathies: an update for neurologists. Arq
945 Neuropsiquiatr. 2022 May;80(5 Suppl 1):238–48.

946 75. Stavropoulos F, Sargiannidou I, Potamiti L, Kagiava A, Panayiotidis MI, Bae JH, et al. Aberrant
947 Mitochondrial Dynamics and Exacerbated Response to Neuroinflammation in a Novel Mouse Model of
948 CMT2A. Int J Mol Sci. 2021 Oct 26;22(21):11569.

949 76. Kerckhove N, Pezet D, Balayssac D. Long-Term Effects, Pathophysiological Mechanisms, and Risk
950 Factors of Chemotherapy-Induced Peripheral Neuropathies: A Comprehensive Literature Review. Front
951 Pharmacol [Internet]. 2017 Feb 24 [cited 2024 Mar 12];8. Available from:
952 https://www.frontiersin.org/journals/pharmacology/articles/10.3389/fphar.2017.00086/full

953 77. Rivera DR, Ganz PA, Weyrich MS, Bandos H, Melnikow J. Chemotherapy-Associated Peripheral
954 Neuropathy in Patients With Early-Stage Breast Cancer: A Systematic Review. JNCI J Natl Cancer Inst.
955 2018 Feb 1;110(2):djx140.

956 78. Jones MR, Urits I, Wolf J, Corrigan D, Colburn L, Peterson E, et al. Drug-Induced Peripheral
957 Neuropathy: A Narrative Review. Curr Clin Pharmacol. 2020 Apr;15(1):38.

958 79. Grisold W, Cavaletti G, Windebank AJ. Peripheral neuropathies from chemotherapeutics and
959 targeted agents: diagnosis, treatment, and prevention. Neuro-Oncol. 2012 Sep;14(Suppl 4):iv45–54.

960 80. Cella D, Huang H, Homesley HD, Montag A, Salani R, De Geest K, et al. Patient-reported
961 peripheral neuropathy of doxorubicin and cisplatin with and without paclitaxel in the treatment of
962 advanced endometrial cancer: Results from GOG 184. Gynecol Oncol. 2010 Dec;119(3):538–42.

963 81. Wu Z, Oeck S, West AP, Mangalhara KC, Sainz AG, Newman LE, et al. Mitochondrial DNA Stress
964 Signalling Protects the Nuclear Genome. Nat Metab. 2019 Dec;1(12):1209–18.

965

Figure 1

A.

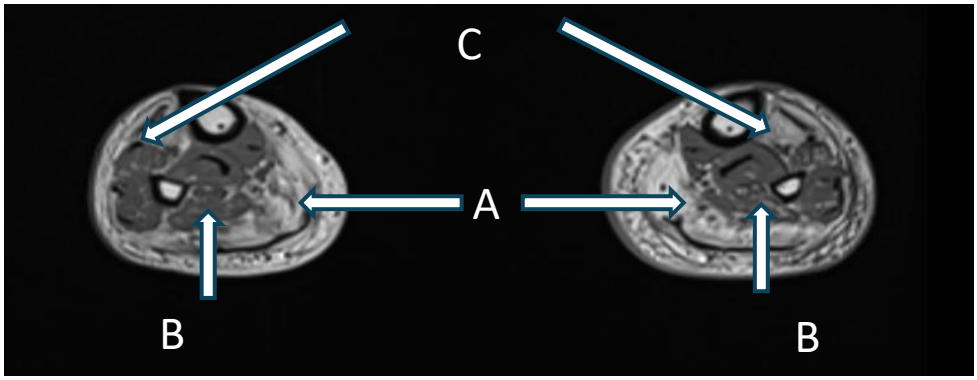

B.

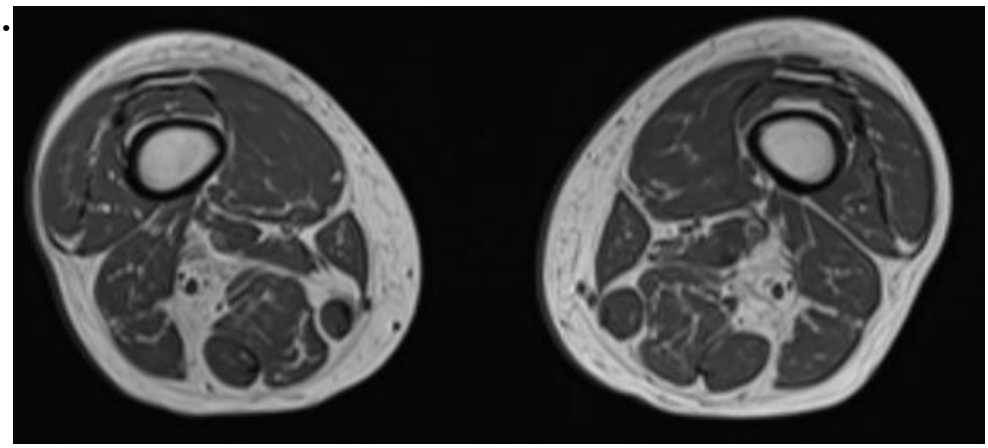

C. (i)

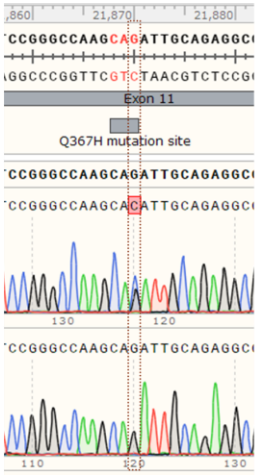

C. (ii)

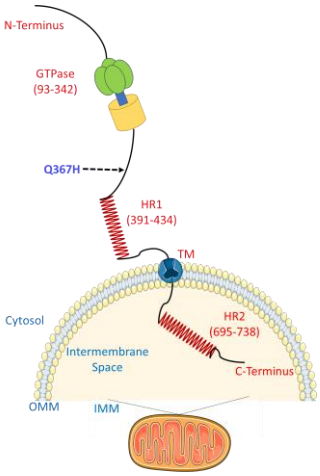

D.

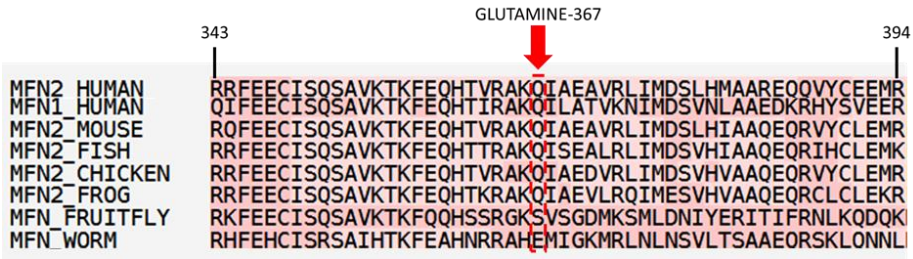

E.

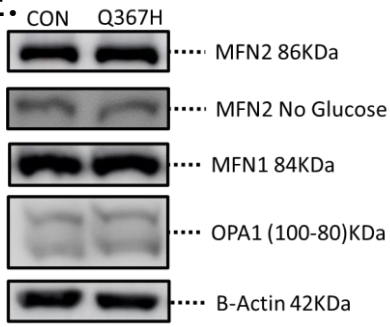

F.

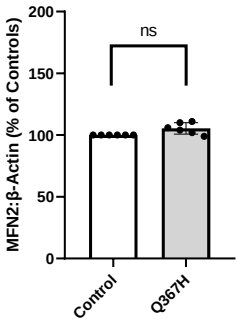

G.

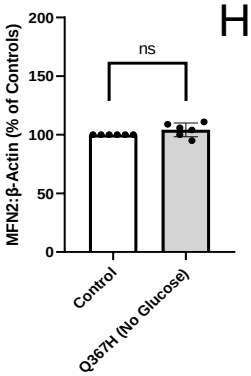

H.

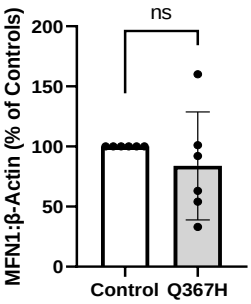

I.

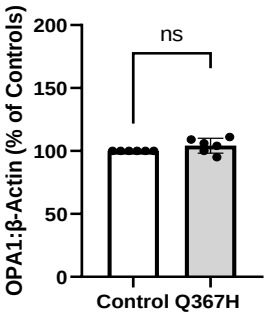

Figure 2

A.

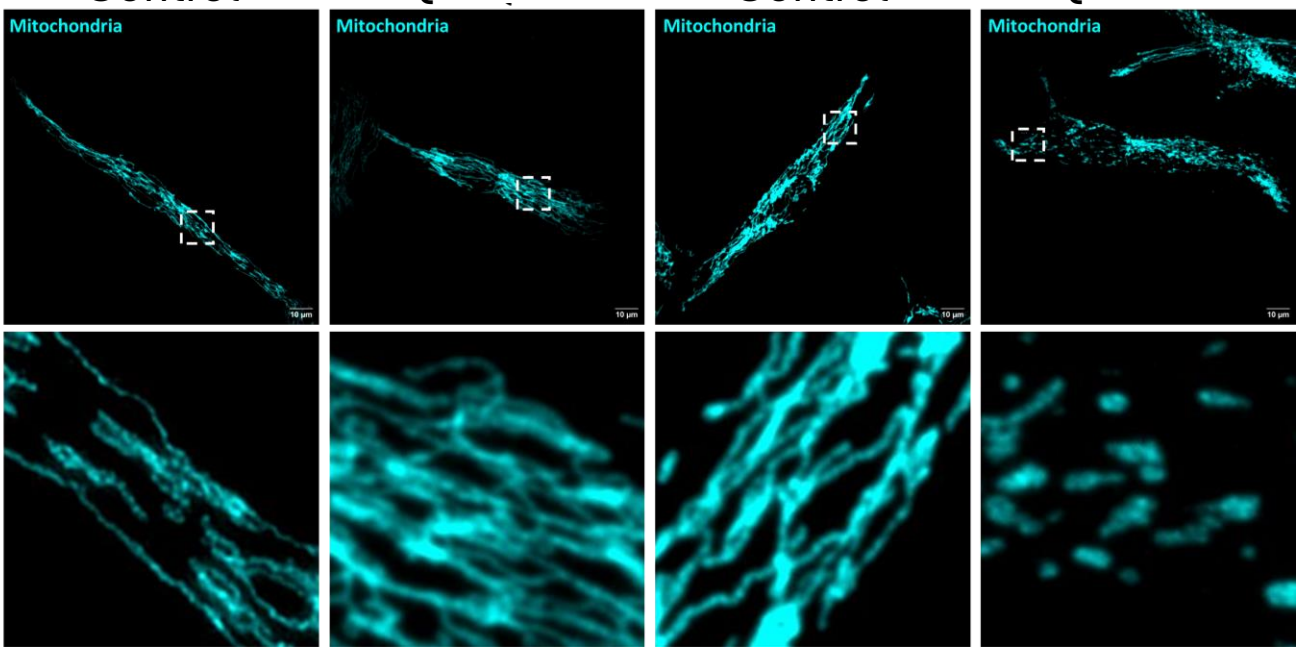

B.

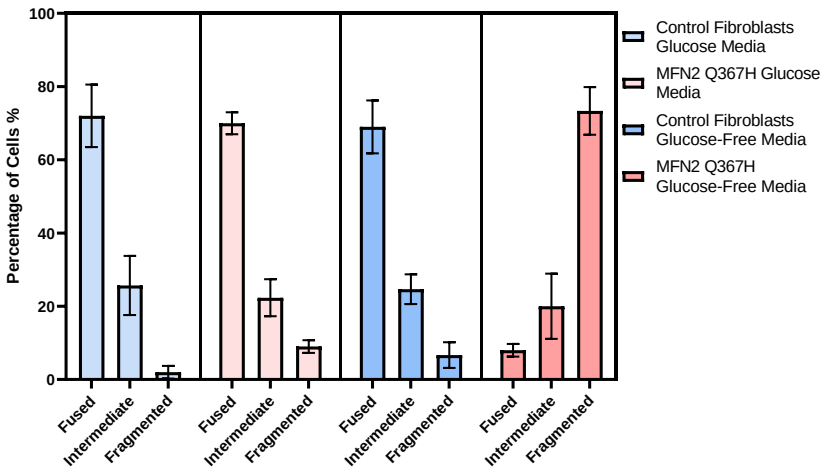

C.

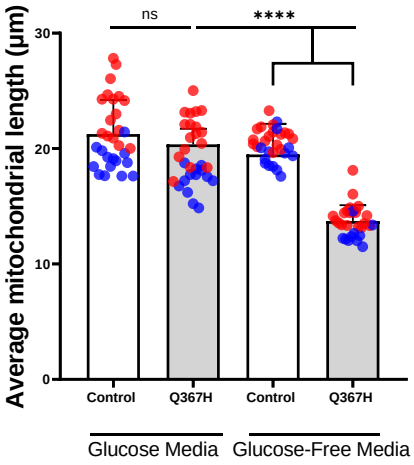

D.

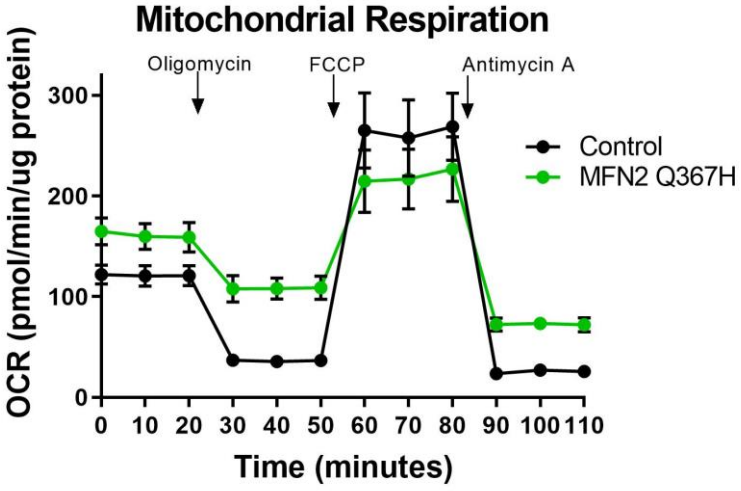

Figure 3

A.

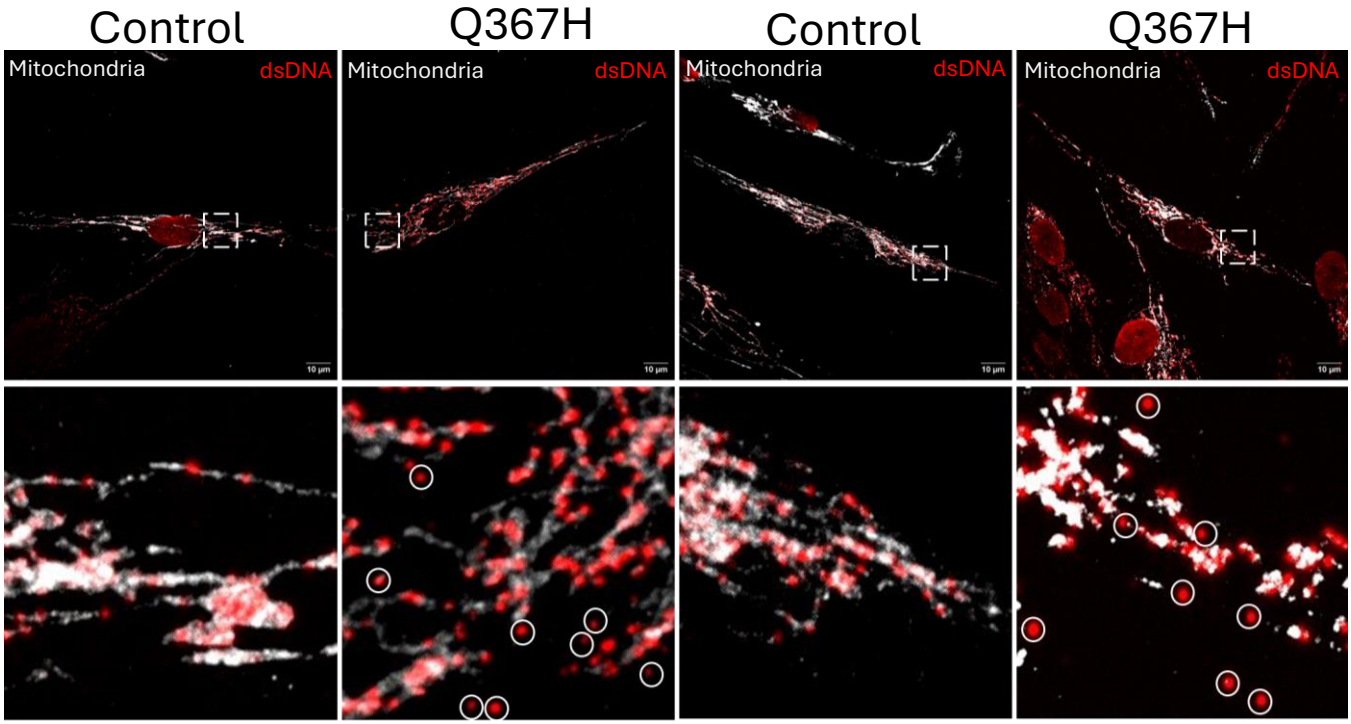

B.

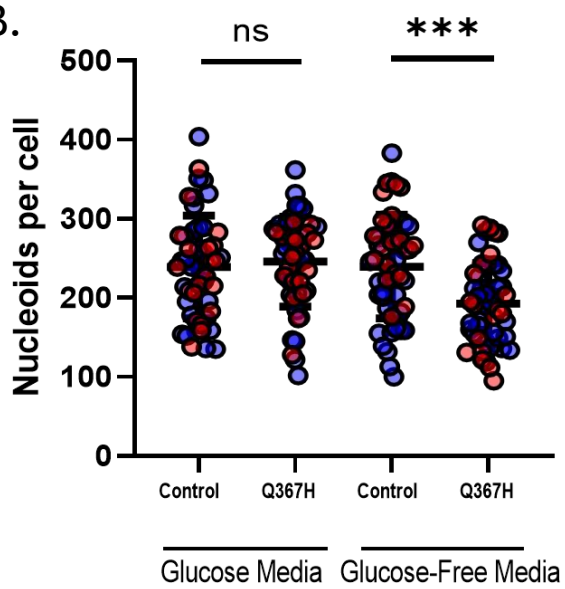

C.

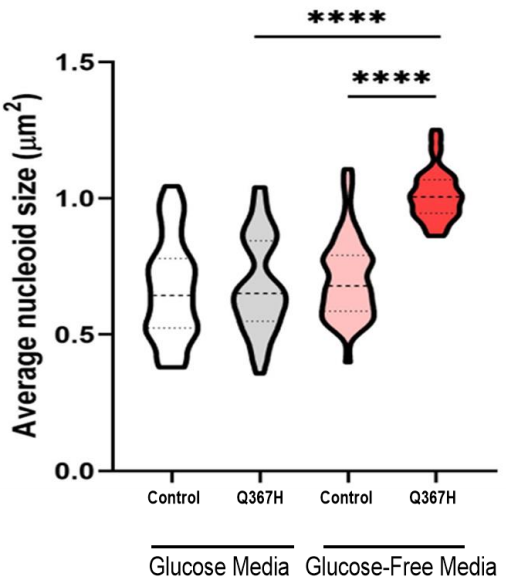

D.

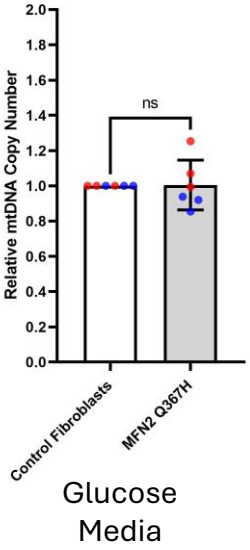

E.

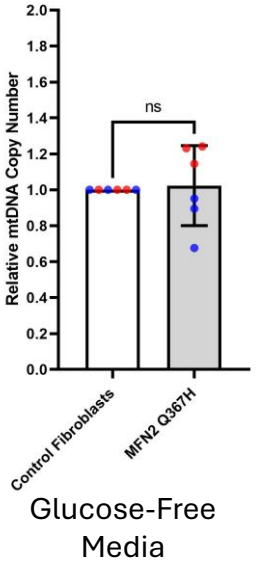

F.

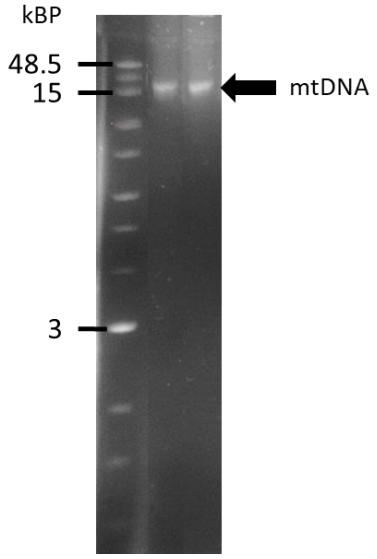

Figure 4

A.

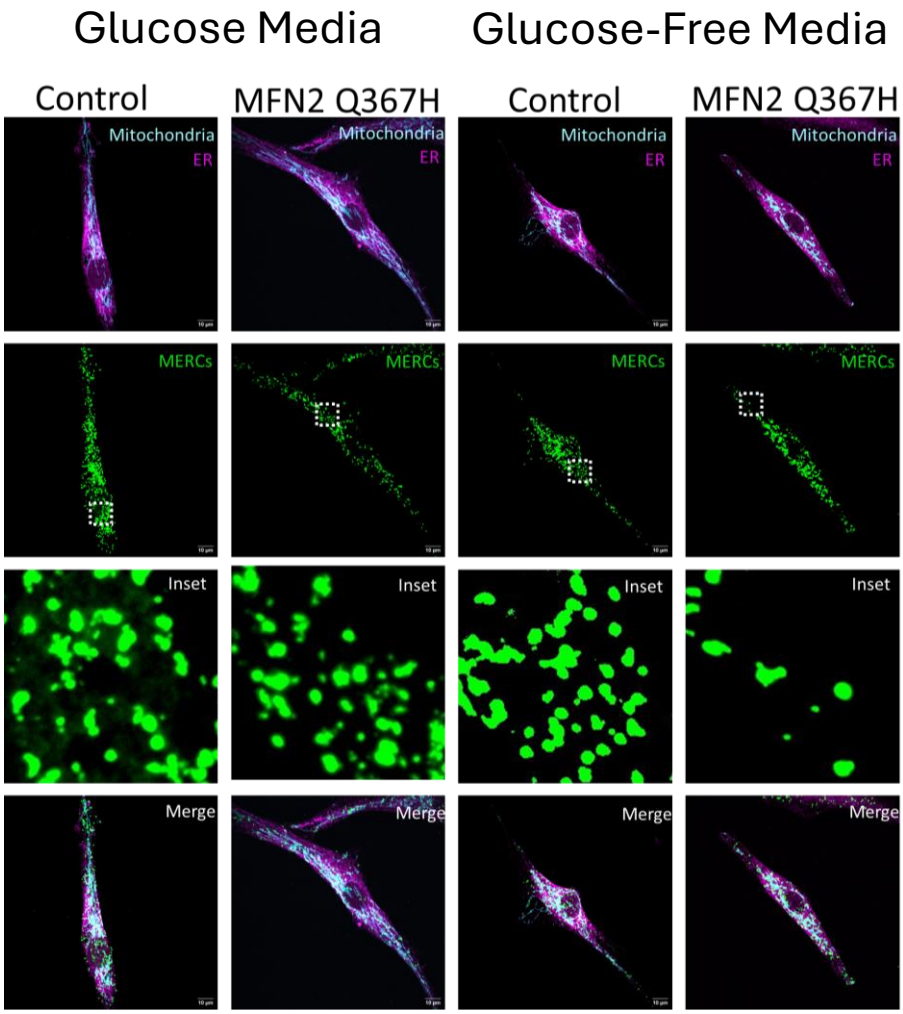

B.

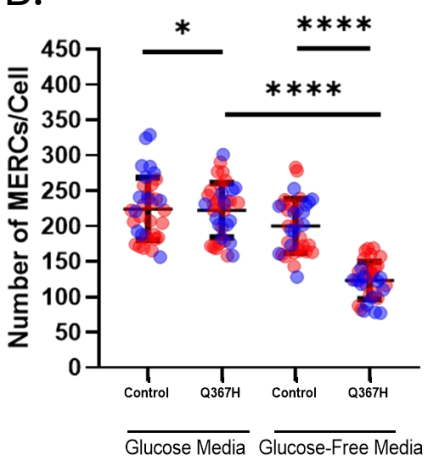

C.

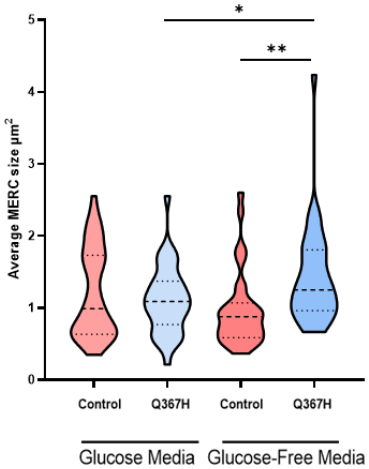

D.

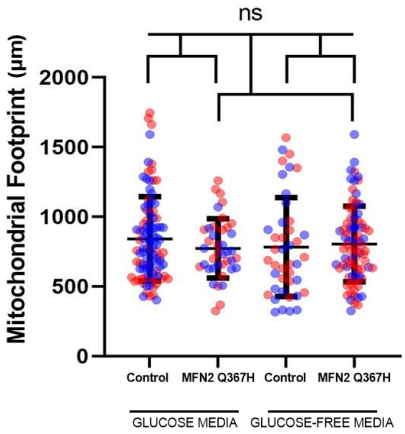

E.

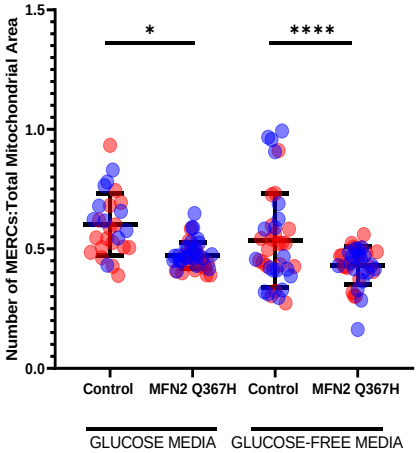

Figure 5

A.

Glucose Media

Control Q367H

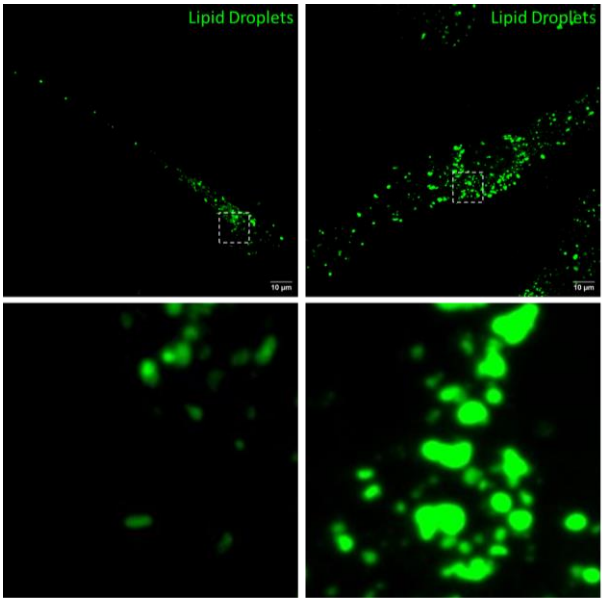

B.

Glucose-Free Media

Control Q367H

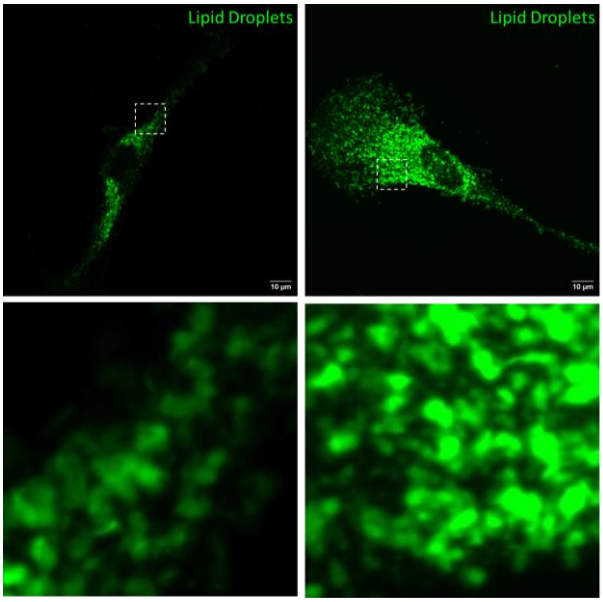

C.

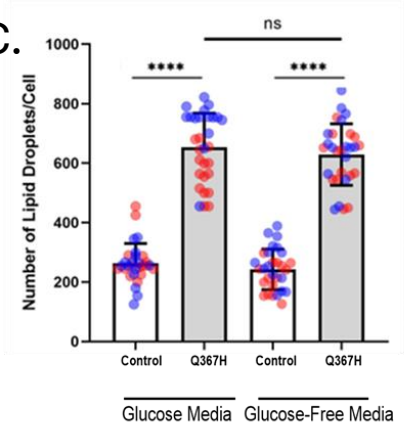

D.

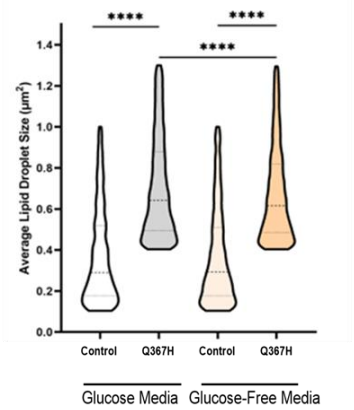

E.

Standard Media Starvation Media

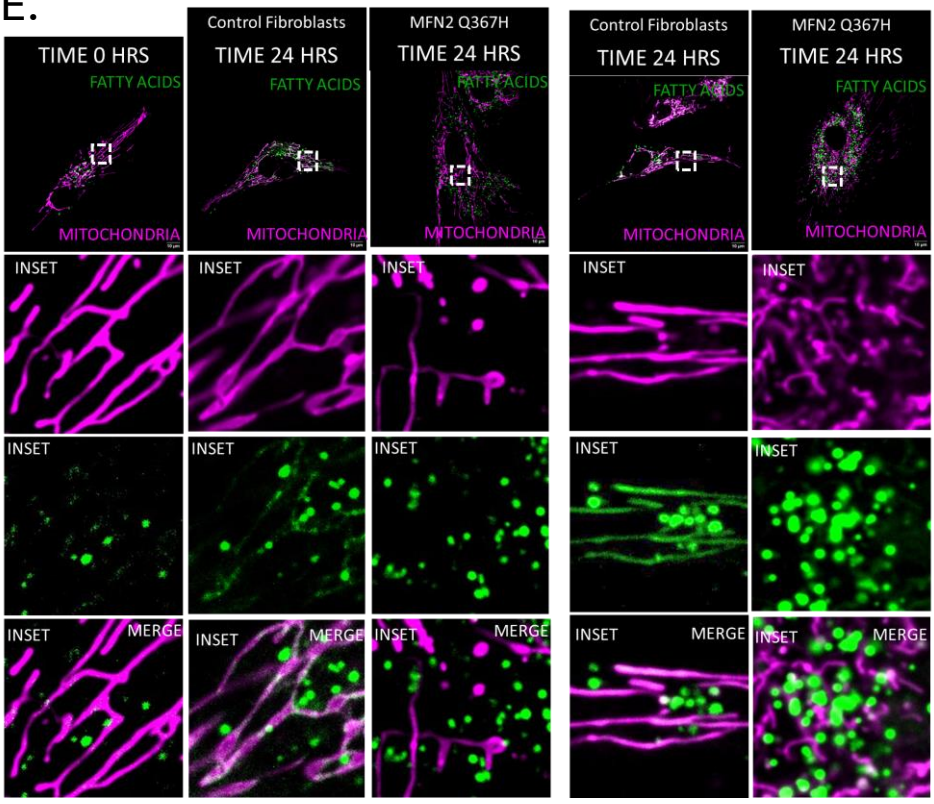

F.

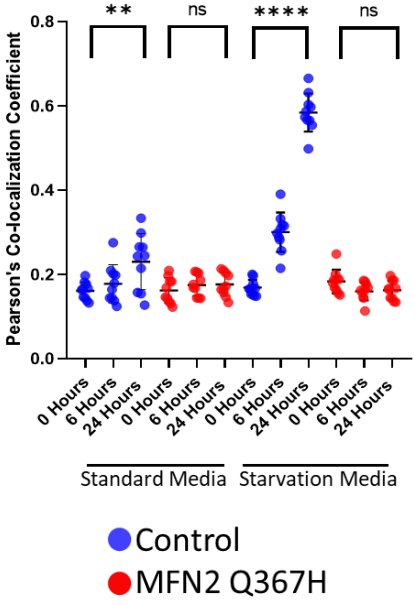

Figure 6

A.

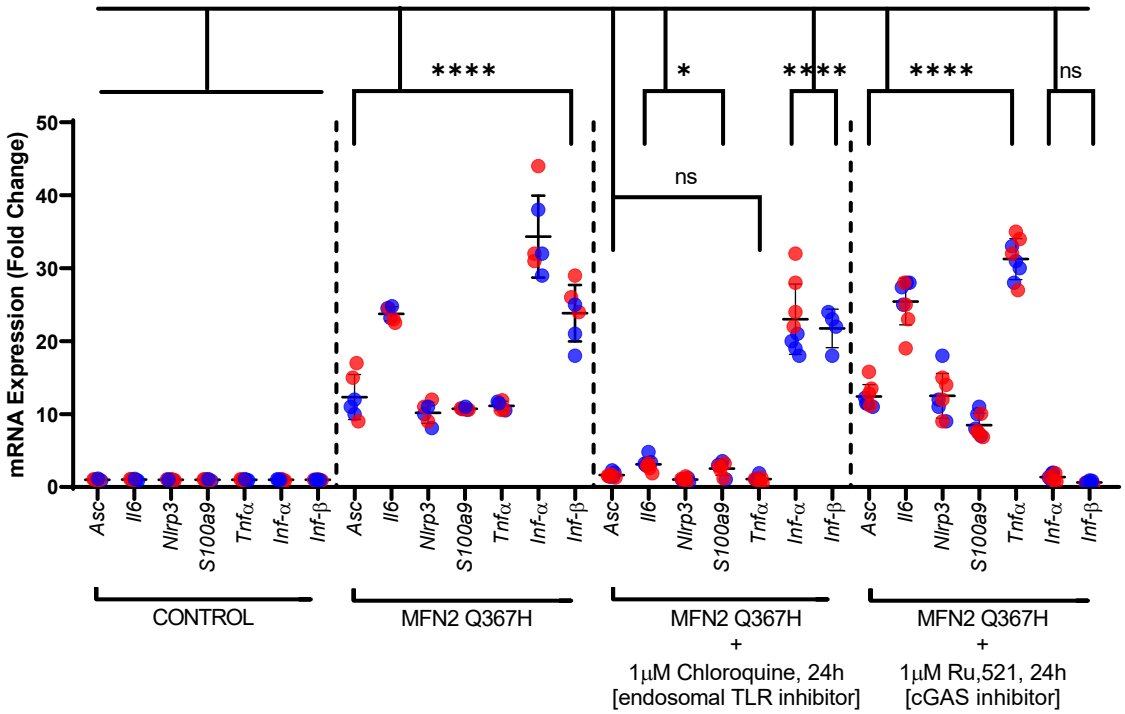

B.

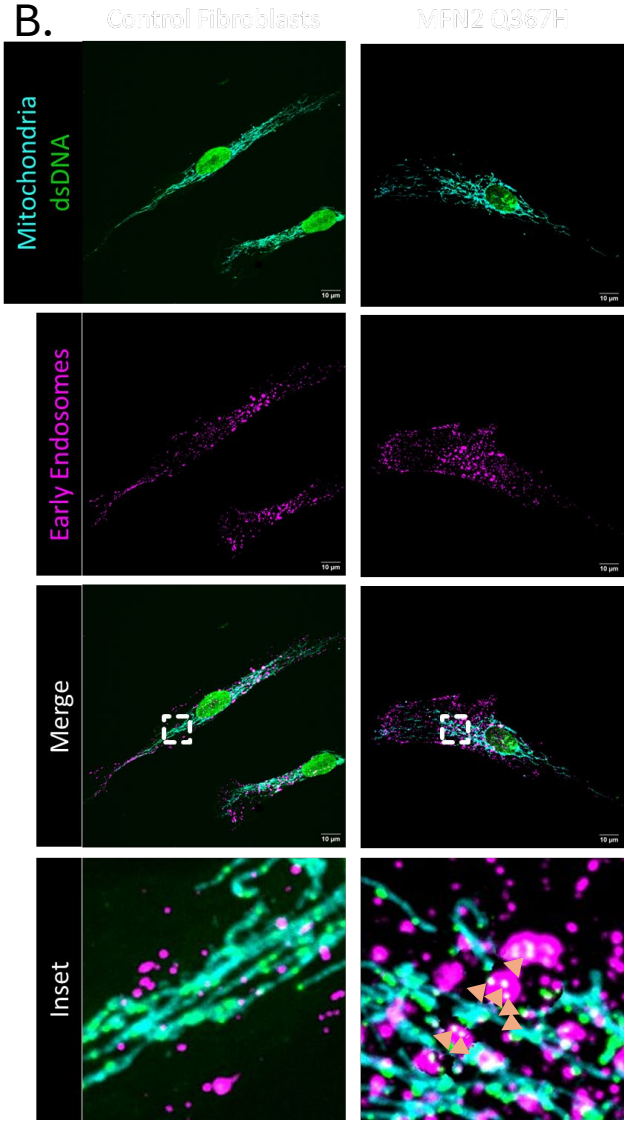

C.

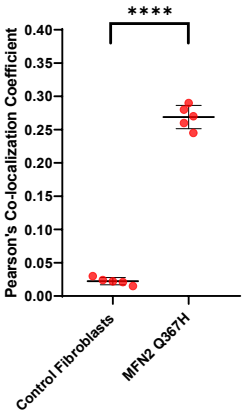

D.

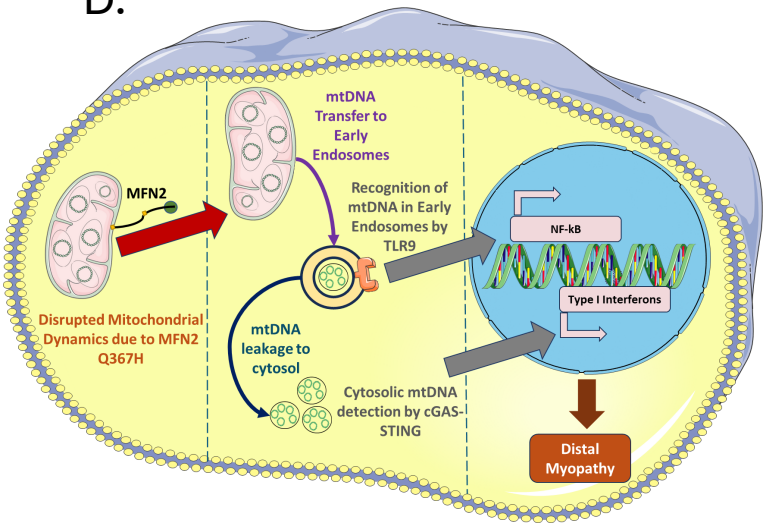

Figure 7

A.

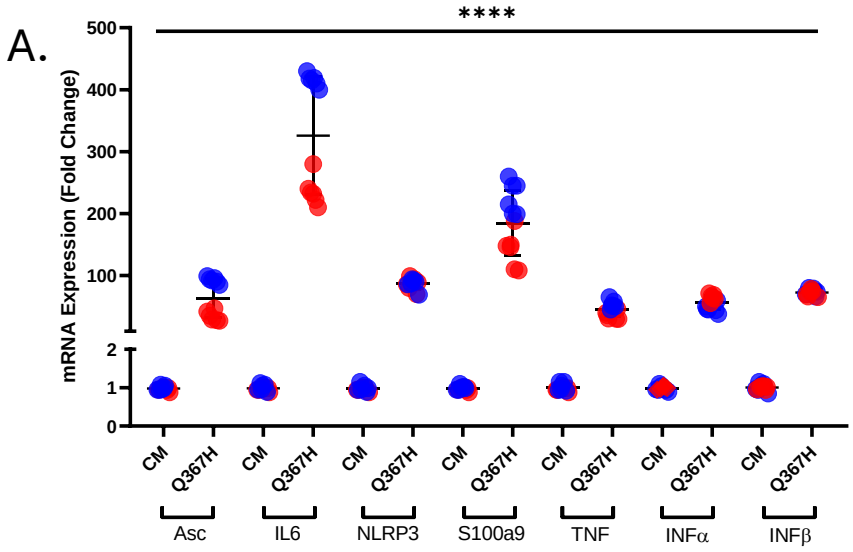

B.

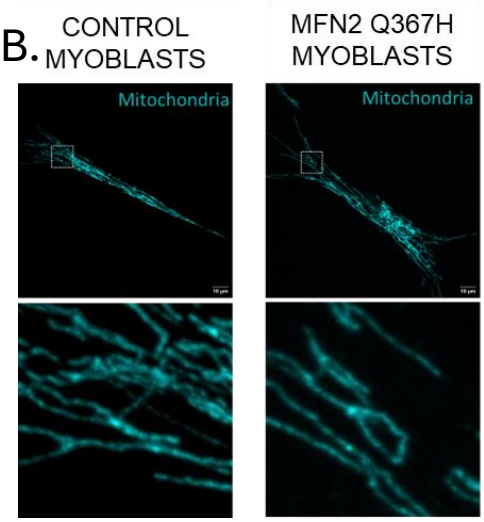

C.

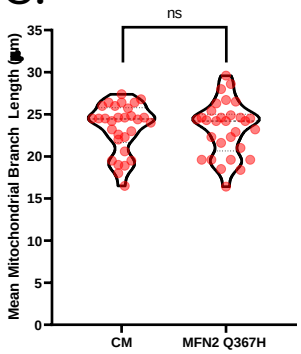

D.

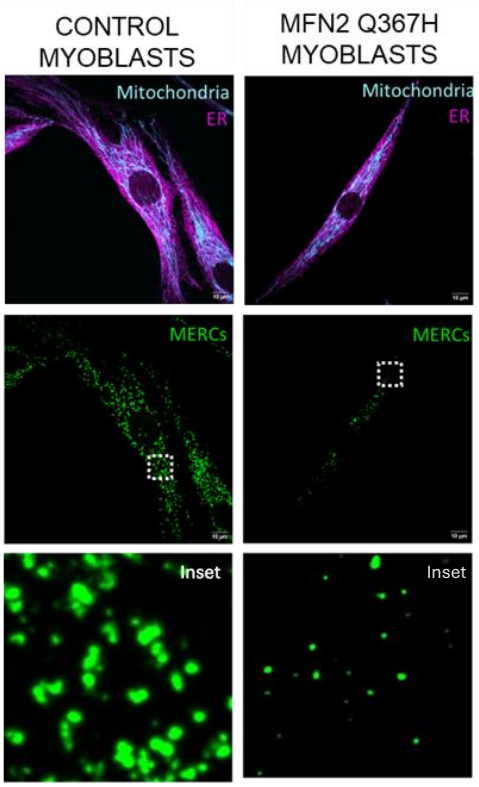

E.

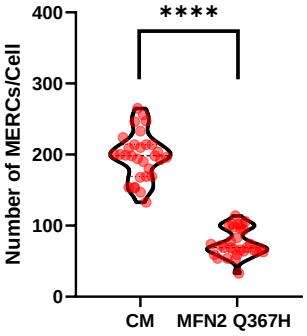

F.

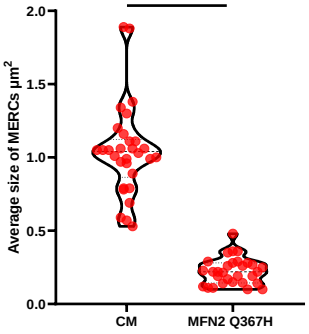

G.

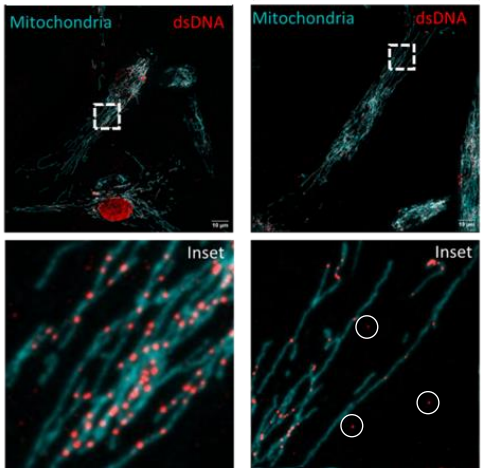

H.

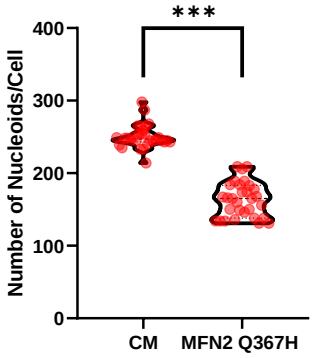

I.

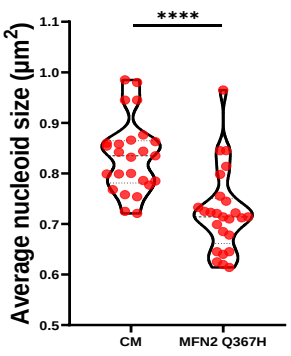

Table 1

Gene	Disease/ Inheritance pattern	Coding variant	Amino acid change	rsID	Max reported MAF	ClinVar	Zygosity	Polyphen 2 prediction	Mutation-taster prediction
MFN2	CMT neuropathy 2A; AD	c.1101G>C	p.Gln367His	rs373211062	0.00024	VUS, conflicting interpretations	Hetero-zygous	B	D
DYSF	LGMD 2B; AR	c.5180G>C	p.Gly1727Ala	rs146153532	1.16E-04	VUS	Hetero-zygous	P	D
SYNE1	EDMD 4; AD/AR	c.9934G>A	p.Asp3312Asn	rs147281213	2.33E-04	VUS	Hetero-zygous	D	D

AD=autosomal dominant; AR=autosomal recessive; B= benign; CMT=Charcot Marie Tooth; D=deleterious; EDMD=Emery Dreyfuss muscular dystrophy; LGMD=limb girdle muscular dystrophy; MAF=minor allele frequency; P=possibly tolerated; VUS=variant of uncertain significance.